frontiers | Frontiers in Marine Science

TYPE Original Research
PUBLISHED 14 January 2025
DOI 10.3389/fmars.2024.1538022

OPEN ACCESS

EDITED BY
Jiangbo Ren,
Guangzhou Marine Geological Survey, China

REVIEWED BY
Sun Ki Choi,
Korea Institute of Ocean Science and Technology (KIOST), Republic of Korea
Bing Li,
First Institute of Oceanography, China

*CORRESPONDENCE
Chunhui Tao
taochunhuimail@163.com

RECEIVED 02 December 2024
ACCEPTED 23 December 2024
PUBLISHED 14 January 2025

CITATION
Yang W, Tao C, Liao S, Zhang H, Zhu C, Li W, Zhang G, Wang X and Wang L (2025) Evolution of a seafloor massive sulfide deposit on axial volcanic ridges: a case study of the Duanqiao hydrothermal field, Southwest Indian Ridge. *Front. Mar. Sci.* 11:1538022. doi: 10.3389/fmars.2024.1538022

Evolution of a seafloor massive sulfide deposit on axial volcanic ridges: a case study of the Duanqiao hydrothermal field, Southwest Indian Ridge

Weifang Yang[1], Chunhui Tao[1,2]*, Shili Liao[1], Huichao Zhang[1,3], Chuanwei Zhu[4], Wei Li[1], Guoyin Zhang[1], Xuefeng Wang[5] and Lisheng Wang[5]

[1]Key Laboratory of Submarine Geosciences, Second Institute of Oceanography, Ministry of Natural Resources, Hangzhou, China, [2]School of Oceanography, Shanghai Jiaotong University, Shanghai, China, [3]Institute of Marine Geology, College of Oceanography, Hohai University, Nanjing, China, [4]State Key Laboratory of Ore Deposit Geochemistry, Institute of Geochemistry, Chinese Academy of Sciences, Guiyang, China, [5]Key Laboratory of Cenozoic Geology and Environment, Institute of Geology and Geophysics, Chinese Academy of Sciences, Beijing, China

The mineralization process below the surface of the seafloor in a hydrothermal field has an important influence on the distribution and enrichment of elements. The Duanqiao hydrothermal field (DHF) is located on the new axial volcanic ridge of the ultraslow-spreading Southwest Indian Ridge. Owing to the limited surface sulfide samples, the metallogenic processes occurring below the seafloor surface such as the element enrichment mechanism and the temporal evolution of the sulfide deposits remain unclear. In this study, we conducted mineral texture, geochemical, ^{230}Th/U dating, and laser ablation inductively coupled plasma mass spectrometer analyses of a drill core containing shallow sulfide deposits to study their evolution process. The results revealed that pyrite is enriched in Mn, Co, As, Mo, Ag, Cd, Sb, Tl, and Pb, chalcopyrite is characterized by high concentrations of Se, Sn, In, As, Ag and Pb, and sphalerite is enriched in Co, Ga, Ge, As, Ag, Cd, Sb, and Pb. The ^{230}Th/U dating data suggested five different mineralization periods during 4,552–2,297 years. Apart from the top and bottom, the core exhibited obvious characteristics of gradual accumulation of mineralization. Results revealed that the variations in the elemental contents of different layers and different types of pyrite were controlled by the interaction of seawater and hydrothermal fluids within the sulfide mound over five different mineralization periods. Compared with other hydrothermal fields on other mid-ocean ridges, DHF pyrite is generally enriched in Zn, Pb, As, Ag, Cd, Mo, and Sb, which might reflect shallow subsurface mixing during different periods of hydrothermal activity.

KEYWORDS

sulfide drill core, trace metal geochemistry, ^{230}Th/U dating, evolution process, Southwest Indian ridge

1 Introduction

Submarine hydrothermal sulfide deposits have been discovered in different tectonic settings, including mid-ocean ridges, back-arc spreading centers and volcanic arcs (Hannington et al., 2005). Approximately 57% of such hydrothermal sulfide deposits are formed in mid-ocean ridge environments (https://vents-data.interridge.org). The scale of the distribution of hydrothermal sulfide deposits is greater on the slow and ultraslow spreading ridges because of the longer duration of hydrothermal activity, deeper magma chambers, and development of detachment faults (Fouquet et al., 1997; Hannington et al., 2011; Petersen and Hein, 2013; Tao et al., 2020). Since 2011, a series of cruises have been conducted by the China Ocean Mineral Resources Research & Development Association to collect samples and data from the Southwest Indian Ridge (SWIR). The geochemical characteristics of ore-forming elements, sources of ore-forming materials, forms of occurrence of precious metals, precipitation mechanisms, and physicochemical conditions of ore formation have been studied using surface sulfide samples obtained from the SWIR (Münch et al., 2001; Tao et al., 2011; Nayak et al., 2014; Zeng et al., 2017; Liao et al., 2018; Cao et al., 2021; Yuan et al., 2018a, Yuan et al., 2018b).

The Duanqiao hydrothermal field (DHF) is located on the new axial volcanic ridges of the ultraslow spreading SWIR. Hydrothermal fields on axial volcanic ridges generally contain only small-scale sulfide deposits, but preliminary exploration of the DHF has revealed that its scale of distribution is larger than that of most hydrothermal fields on either fast- or slow- spreading ridge axis (Hannington et al., 2011; German et al., 2016; Yang et al., 2023). However, its potential mineral resources are lower than those of some ore deposits developed on the northern Mid-Atlantic Ridge, e.g., s Puy des Folles, and Krasnov hydrothermal fields (Cherkashov et al., 2023). Previous studies have demonstrated that a sufficient heat source, stable channels, and alternating intensity of magma supply on a ridge axis might explain the large-scale mineralization in the DHF (Li et al., 2015; Jian et al., 2017; Tao et al., 2020; Chen et al., 2021). Earlier analyses revealed that the contents of Pb (263-2630 ppm), As (234-726 ppm), Sb (7.32-44.3 ppm), and Ag (35.2 to >100 ppm) in the DHF surface sulfides are relatively high, and substantially higher than those of the Longqi, Yuhuang, and Tianzuo hydrothermal fields on the SWIR and those of most magmatic hydrothermal fields on slow- spreading ridge axis (Fouquet et al., 2010; Yang et al., 2023). The current understanding of sulfide mineralization associated with the SWIR is based on the analysis of surface samples, but the metallogenic processes occurring below the seafloor surface have yet to be investigated.

Through analysis of sulfide drilling samples collected by the International Ocean Discovery Program and Blue Mining programs, the three-dimensional structure and composition of sulfide deposits can be obtained. The mineralization process occurring below the surface of the seafloor in a hydrothermal field has an important influence on the distribution and enrichment of elements. Current research on drilling samples is limited to the TAG and Snake Pit hydrothermal fields of the Mid-Atlantic Ridge, and the Bent Hill hydrothermal zone of the Middle Valley (Petersen et al., 1998, Petersen et al., 2000; You and Bickle, 1998;Zierenberg et al., 1998). The internal structure of the Semenov-5 hydrothermal field has also been studied through mineralogical and chemical analyses of different parts of the sulfide deposits (Firstova et al., 2022). The formation of submarine hydrothermal sulfide proceeded via periodic mineralization, and its accumulation process included chimney growth, collapse accumulation, and hydrothermal fluid filling and metasomatism in open spaces (Humphris et al., 1995; Zierenberg et al., 1998; Graber et al., 2020). In recent years, the application of *in situ* and high-spatial-resolution mineral chemical analysis techniques has led to important advances in both elucidation of element migration and enrichment mechanisms, and determination of the mode of occurrence of modern and ancient seafloor hydrothermal sulfides (Butler and Nesbitt, 1999; Choi et al., 2023; Cook et al., 2009; Keith et al., 2016a; Li et al., 2018, Li et al., 2024; Ren et al., 2021; Wohlgemuth-Ueberwasser et al., 2015; Wang et al., 2017; Yuan et al., 2018a, Yuan et al., 2018b). The study of hydrothermal sulfide chronology is vitally important in determining the history of the formation and evolution, mineralization scale, accumulation rate, and hydrothermal activity of sulfide deposits (Lalou and Brichet, 1982, Lalou and Brichet, 1987; Lalou et al., 1993, Lalou et al., 1996; Kuznetsov et al., 2015; Cherkashov et al., 2017; Jamieson et al., 2014, Jamieson et al., 2023).

This study used drill cores of surface sulfide mounds collected from the DHF to systematically analyze the sulfide mineralogy, bulk geochemistry, and *in situ* geochemical compositions of pyrite, chalcopyrite, and sphalerite and to perform ^{230}Th/U dating. Based on the results, the mineralization characteristics and the controlling factors on trace elements were investigated. The findings of this study support systematic comprehension of both the metallogenic element enrichment mechanism and the evolution process of the DHF from a spatiotemporal perspective.

2 Geological setting

The SWIR extends from the Bouvet Triple Junction in the South Atlantic Ocean to the Rodrigues Triple Junction in the Indian Ocean (Figure 1A). It is characterized by ultraslow spreading, with a full spreading rate of 1.4–1.8 cm/yr (Dick et al., 2003). The DHF is located between the Indomed and Gallina transfer faults, with the central volcano at 50°28′ E in segment#27 (Figure 1B) (Cannat et al., 1999). The SWIR is expanding symmetrically, and the oceanic crust is 9.5–10.2 km thick, i.e., approximately 3 km thicker than the average thickness of oceanic crust (Li et al., 2015; Jian et al., 2017; Liu and Buck, 2018). The DHF is on the axial ridge high at a depth of approximately 1,700 m (Tao et al., 2012). It is a typical magma-supply type hydrothermal field, evidently different from the Longqi and Yuhuang hydrothermal fields that have poor magma supply and are controlled by detachment faults (Tao et al., 2012; Tao et al., 2020; Yu et al., 2021). The sufficient magma supply, alternating intensity of magmatic activity, and large numbers of normal faults and tectonic fractures suggest that the DHF is well suited to the development of sulfide deposits.

The DHF was discovered in 2009 during the DY20 cruise. Since then, several subsequent cruises conducted in this area have

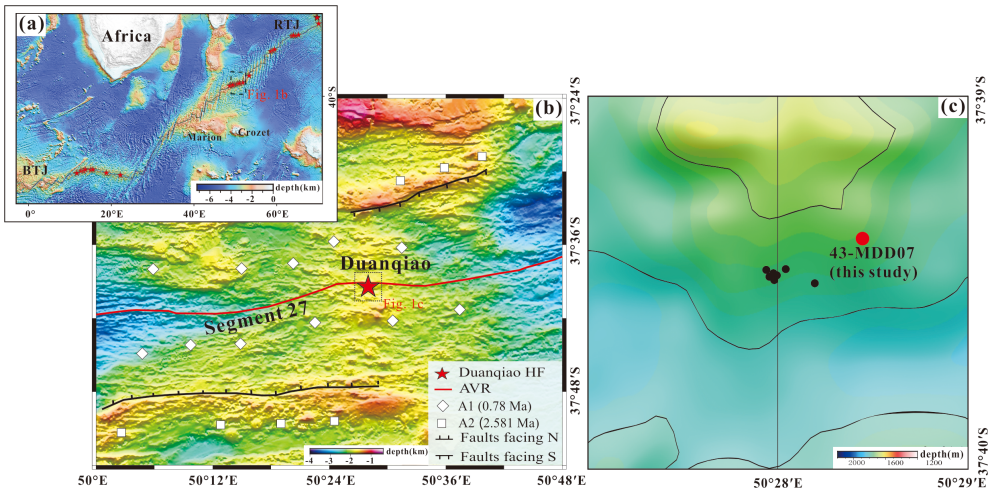

FIGURE 1
Geological setting and bathymetry of the study area. **(A)** Geotectonic setting and topography of the SWIR. **(B)** Shipboard bathymetric map of the segment #27 of the SWIR (Revised form Yang et al., 2023). **(C)** The sulfide drilling locations. The black and red dots represent all the drilling locations. The red dot represents the sample station discussed in this paper. All the normal fault line and the age of ocean crust in panel **(B)** are from Chen et al. (2021). The red stars in panel **(A)** represent the hydrothermal fields along the SWIR. Abbreviations: BTJ, Bouvet Triple Junction; RTJ, Ridge Triple junction, AVR, Axial volcano ridge.

collected abundant geological samples that include basalts, sulfides, and opals (Tao et al., 2012). Preliminary studies of the DHF sulfide distribution revealed that it consists of two main areas of sulfide deposition.

Massive sulfides and relict chimney fragments are found on the surface or adjacent to the mound. The host rocks are basalts and basaltic breccias, whereas sediments are distributed along slopes or in areas of low terrain (Yang et al., 2023). During the DY30, DY34, DY43 and DY65 cruises, sulfide drilling sampling was performed and eight drilling cores were obtained (Figure 1C). The maximum drilling depth was 10 m, which initially revealed the mineralized zonation characteristics of the sulfide in the area.

3 Samples and analytical methods

3.1 Sample collection and description

The representative DHF sulfide samples (from drill core 43-MDD07) used in this study were collected from the sulfide mound using shallow drilling equipment during the DY43 cruise of R/V *Xiayanghong* 10 in 2017. The entire core used in this study comprises Fe-rich sulfides. The drilling depth was 2 m, but the obtained sample length was 99 cm, the core recovery was 49.5%. Owing to core collapse, only an 8-cm sample of sulfide breccia was obtained from the top 1m. And 91-cm sample of sulfides was obtained from the bottom 1m (Figure 2A). Of the bottom 1 m, the uppermost part of the drill core comprises sulfide breccias of pyrite, marcasite, sphalerite, amorphous silica and chalcopyrite. The underlying mineralized sulfide comprises zones of massive pyrite – marcasite – sphalerite – silica (108-117 cm), massive pyrite – chalcopyrite – sphalerite – marcasite – silica (117-151 cm), massive pyrite – chalcopyrite – sphalerite – silica (151-173 cm), massive pyrite – sphalerite – marcasite – silica (173-193 cm), massive pyrite – silica – marcasite (193-199 cm) (Figures 2B–F).

3.2 Analytical methods

Mineral and textural analyses were conducted at the Key Laboratory of Submarine Geosciences (Ministry of Natural Resources, Hangzhou, China). All samples were examined as polished thin sections using a reflected and transmitted light polarizing microscope (Zeiss AXIO Scope A1).

Micro-drilling was also conducted at the Key Laboratory of Submarine Geosciences using Proxxon MICROMOT drilling equipment to obtain geochemical and chronological subsamples. Thirteen micro-drilled subsamples were selected for determination of bulk geochemical concentrations at the ALS Laboratory in Guangzhou (China). Trace elements were analyzed using an inductively coupled plasma mass spectrometer (ICP-MS; POEMS III ICP-MS, Thermo Jarrell Ash Ltd., USA). The analytical error of the trace elements data was <0.05%.

Trace element concentrations of pyrite, sphalerite and chalcopyrite from the DHF were determined with a laser ablation (LA)-ICP-MS at Nanjing FocuMS Technology (China), using a Teledyne Cetac Technologies Analyte Excite LA system (Bozeman, Montana, USA) coupled to an Agilent Technologies 7700x quadrupole ICP-MS (Hachioji, Tokyo, Japan). A 193 nm ArF excimer laser, homogenized by a set of beam delivery systems, was focused on mineral surface with a fluence of 6.06J/cm^2. The ablation protocol employed a spot diameter of 40 μm at a 6-Hz repetition rate for 40 s (equating to 280 pulses). Further details of the operating conditions and methods used can be found in Hou et al. (2009) and Gao et al. (2013). The United States Geological Survey polymetallic sulfide pressed pellet *MASS-1* and synthetic

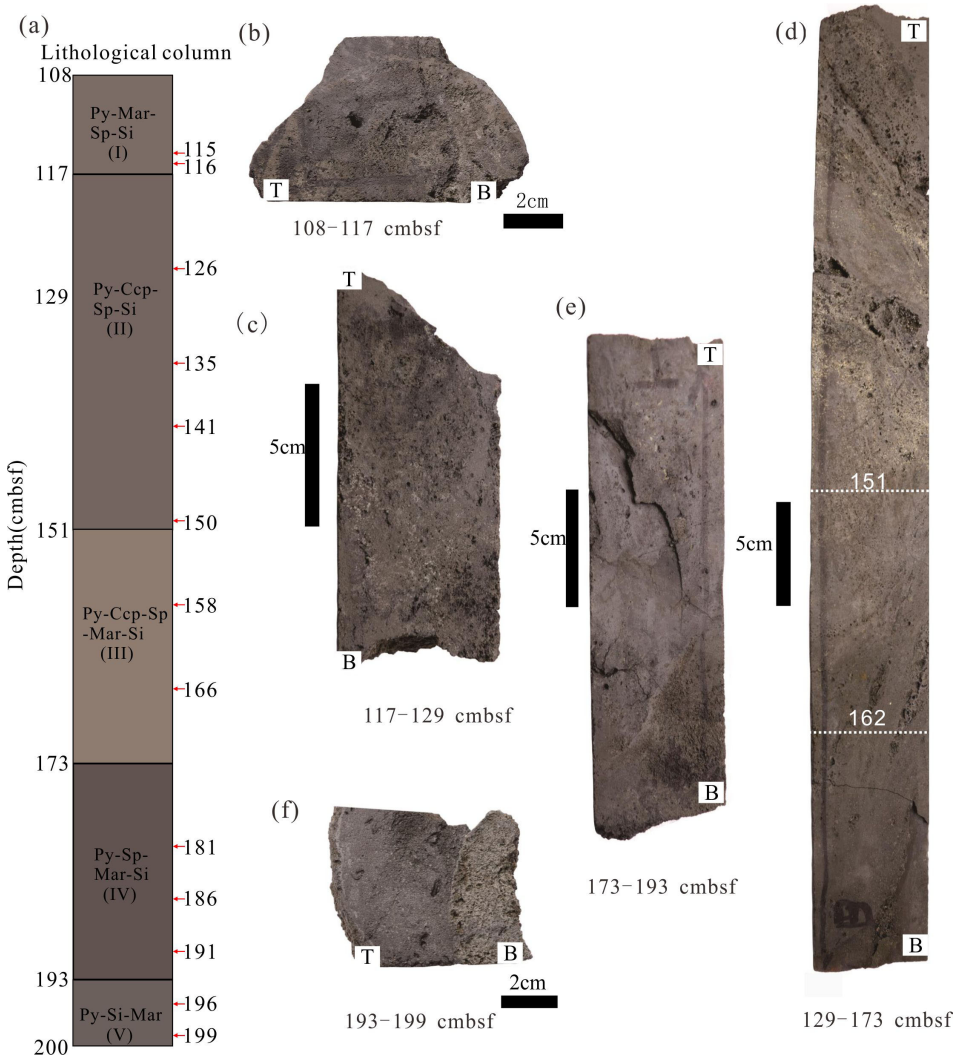

FIGURE 2
Photographs of cross sections of drill core (43-MDD07) from the DHF and original samples used for analysis. **(A)** the lithological column of the core (unit: cm); **(B)** massive pyrite – marcasite – sphalerite – silica; **(C)** massive pyrite – chalcopyrite – sphalerite – marcasite – silica; **(D)** massive pyrite – chalcopyrite – sphalerite – marcasite – silica and massive pyrite – chalcopyrite – sphalerite – silica; **(E)** massive pyrite – sphalerite – marcasite – silica; **(F)** massive pyrite – silica – marcasite. bsf: below seafloor. The red arrow in Figure a represents the sampling location for bulk chemistry and chronology analysis. T and B in Figure b-f represents top and bottom respectively. Mineral abbreviations: Py, pyrite; Ccp, chalcopyrite; Sp, sphalerite; Mar, Marcasite; Si, silica.

basaltic glasses *GSE-1G* were used as standards to calibrate the elements contents of the sulfides. Raw data reduction was performed offline by ICPMSDataCal software using a 100%-normalization strategy without applying an internal standard (Liu et al., 2008). Precision and accuracy were better than ± 10%.

Seven micro-drilled subsamples were selected for ^{230}Th/U dating. The chemical separation of U and Th, together with the MS analysis, were performed at the Uranium Series Chronology Laboratory of the Institute of Geology and Geophysics, Chinese Academy of Sciences. The chemical separation procedures and MS analysis adopted were similar to those described in Yang et al. (2017) and Wang et al. (2021). A standard (GBW04412) was analyzed to verify the accuracy and precision of the ^{230}Th/U dating, providing precision better than 95%. The best age accuracy can be better than 5‰ (Cheng et al., 2013). All the results were within 2σ uncertainty, unless indicated otherwise.

4 Results

4.1 Mineralogy and paragenesis of sulfides

From the microscopically observed characteristics of the drilling core in different mineralized zones, it was determined that the core comprised mainly Fe-rich sulfide, and that the mineral assemblage was pyrite, sphalerite, chalcopyrite, marcasite, and amorphous silica. Among those minerals, pyrite was most abundant, although sphalerite and chalcopyrite were also common.

10.3389/fmars.2024.1538022

Pyrite was found present throughout the core. Four paragenetic types with distinct textures were recognized: granular pyrite (Py1), late overgrowths of coarse granular pyrite (Py2), colloform and/or dendritic pyrite (Py3), and euhedral pyrite (Py4). Granular Py1 and colloform Py3 were common through the core. Granular Py1, coarse-grained Py2 and chalcopyrite particles were found in the inner wall of the hydrothermal channel, and the pyrite shows obvious growth zoning (Figure 3A). Colloform Py3 and marcasite were also common in the top and the bottom parts of the core. Colloform Py3 was often associated with marcasite (Figure 3G). Colloform Py3 also often surrounded by

Sphalerite in the massive Py-Sp layer of the core (129–151 cmbsf) (Figure 3E). Dendritic pyrite, which generally occurred because of sphalerite intergrowth, was common in the silicified Py layer (173–193 cmbsf) (Figure 3G). Early granular Py1 was replaced by late recrystallized coarse granular Py2 and disseminated with globular Py3 in amorphous silica (173–193 cmbsf) (Figure 3H). Euhedral Py4 exhibited sharp, well-defined crystal boundaries and discrete well-formed euhedral shapes, and it was commonly replaced by chalcopyrite in the massive Py-Sp layer of the core (162–173 cmbsf) (Figure 3F).

Sphalerite often occurred with massive textures in most samples of the core. In the upper part and the lower-middle part of the core, the content of sphalerite was obviously higher than that in the central part. Sphalerite (Sp2) surrounding pyrite indicates a precipitation after pyrite and can occur as laminated colloform textures in the inner wall of the fluid conduit in the middle part of the core (151–162 cmbsf) (Figure 3E). In the top of the core (108–117 cmbsf), massive sphalerite (Sp1) is commonly associated with colloform Py3 (Figure 3C). Massive sphalerite often replaced chalcopyrite and pyrite (Figure 3I) and was found to have a mutual replacement relationship with pyrite (Figure 3G) in the middle and bottom of the core.

Chalcopyrite was often found with granular textures, and it occurred mainly as a replacement of sphalerite and pyrite (Figures 3D, E, I). Chalcopyrite was also often found in the inner wall of the fluid conduit in the top of the core (Figure 3A). In the central part of the core, the content of chalcopyrite was higher than that in the in the upper and lower parts of the core.

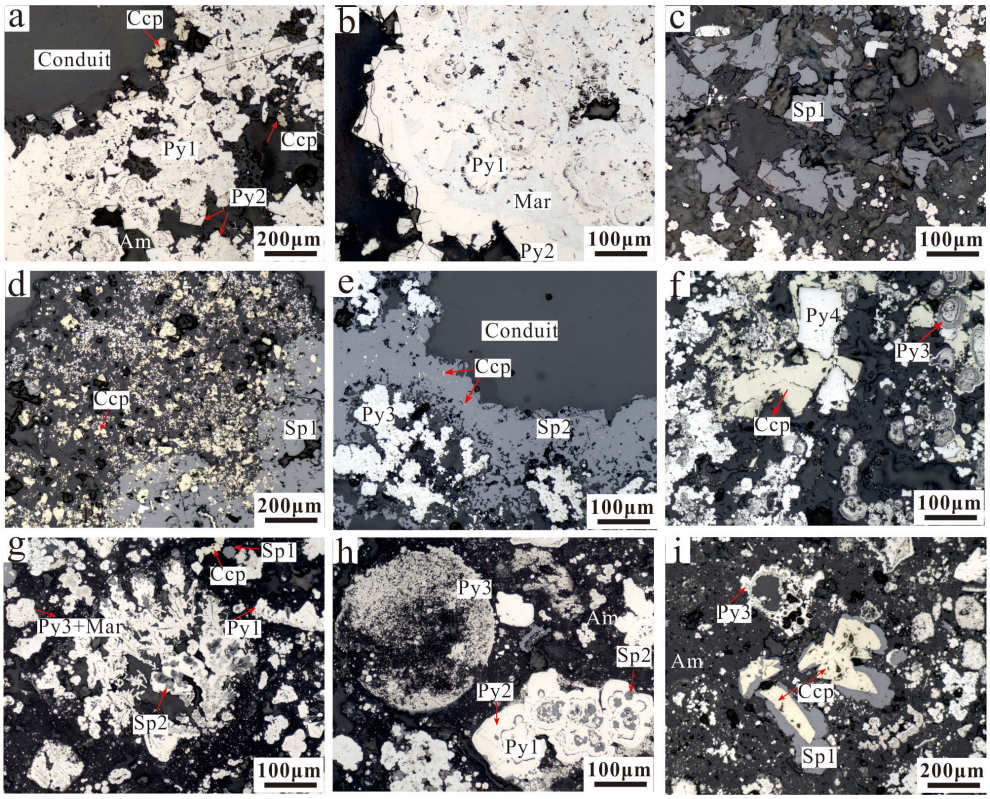

FIGURE 3
Representative photomicrographs of the sulfide core samples of the DHF. **(A)** The coarse-grained pyrite and chalcopyrite particles were found in the inner wall of the hydrothermal channel, the pyrite multiple generations of grained Py1 and Py2 (108– 117 cmbsf); **(B)** Marcasite was often associated with grained Py1 and Py2 (108–117 cmbsf); **(C)** Massive sphalerite (108–117 cmbsf); **(D)** Chalcopyrite was dispersed in massive sphalerite (Sp1) and pyrite (129–151 cmbsf); **(E)** Sphalerite was distributed around the hydrothermal channel and associated with pyrite 3 (151–162 cmbsf). **(F)** Chalcopyrite was filled in the gap of colloform pyrite (Py3) and replaced euhedral pyrite (Py4) (162–173cmbsf); **(G)** Dendritic pyrite (Py3) generally occurred as colloform sphalerite (Sp2) replacement structure (173–193 cmbsf); **(H)** Early colloform pyrite was replaced by late recrystallized pyrite and disseminated with globular pyrite in amorphous silica (173–193 cmbsf); **(I)** Massive sphalerite (Sp1) replaced chalcopyrite and recrystallized pyrite replaced early colloform pyrite (Py3) (173–193 cmbsf). Mineral abbreviations: Py, pyrite; Ccp, chalcopyrite; Sp, sphalerite; Mar, marcasite; Am, amorphous silica.

Marcasite was often associated with grained Py1, Py2 and colloform Py3 in the upper and bottom layer of the core (Figures 3B, G).

4.2 Bulk chemistry

The geochemical compositions of the samples, presented in Table 1, were found characterized by high Fe content (19.31-41.75 wt.%, avg. 26.23 wt.%, n=13) and variable Zn content (0.47–19.54 wt.%, avg. 5.17 wt.%). The Zn content in the 126- and 186-cm layers was evidently higher than that in other layers. Compared with Fe and Zn, the content of Cu was low (0.11–8.69 wt.%, avg. 2.02 wt.%, n=13). The Pb, As, and Cd contents were 142.45–755.24 ppm (avg. 235.17 ppm), 150.13–797.20 ppm (avg. 314.38 ppm), and 25.17–920.01 ppm (avg. 212.09 ppm), respectively. The Co, Mo, and Mn contents were 21.25–213.68 ppm (avg. 87.06 ppm), 37.53–161.24 ppm (avg. 79.77 ppm), and 25.17–124.76 ppm (avg. 65.03 ppm), respectively. In contrast, the contents of Ag (1.83–50.35 ppm, avg. 18.73 ppm, n = 9), Sb (17.00–85.36 ppm, avg. 34.46, n = 8), Ni (4.71–14.25 ppm, avg. 8.10 ppm, n =11), and Se (20.85–43.08 ppm, avg. 30.14 ppm, n = 5) were relatively low compared with those of Pb, As, and Cd. The contents of trace elements showed considerable variation with depth. It is evident from Figure 4 that the variations trend in the contents of Cu and Co were similar. And the Fe, Pb, Ag, and As presented the same variations trend. However, it is notable that at the bottom of the core, the Fe content exhibited a maximum, the Cu and Co contents were markedly reduced, and the Pb, Ag, and As contents were particularly high (Table 1).

4.3 LA-ICP-MS data

4.3.1 Pyrite

A total of 144 spot analyses were performed on different types of pyrite at different depths within the core. The range of trace element concentrations was found to fall into five main groups: <1, 1–10, 10–100, 100–1000, and >1000 ppm (Table 2). Elements found to have the highest concentration were Cu (avg. 1,237 ppm) and Zn (avg. 4,486 ppm). The average contents of Co, As, and Pb (i.e., 151, 417, and 992 ppm, respectively) were in the range 100–1,000 ppm with notable outliers (up to 1,669 ppm Co, 3,998 ppm As, and 6,862 ppm Pb). The average contents of Mn, Mo, Ag, Cd, Sb, and Tl were in the range 10–100 ppm with notable outliers (up to 1027 ppm Mn, 572 ppm Mo, 474 ppm Ag, 1283 ppm Cd and 884 ppm Tl). The average contents of V, Cr, Ni, Ga, Ge, Se and In were in the range 1–10 ppm (up to 257 ppm Ga, 376 ppm Ge and 144 ppm Se). The average contents of Ti, Te, Ba, W, Au and Bi were all <1 ppm.

The contents and compositions of the trace elements in different types of pyrite at different depths within the core were evidently different (Supplementary Table S1). The downhole distribution of selected trace elements is shown in Figure 5. The average values of Co, Se, As, Pb, and Cd of pyrite showed a trend of gradual decline. However, the contents of Co and Se were relatively high in the 162–173 cmbsf layer, whereas the content of Cd was relatively high in the 173–193 cmbsf layer. The average values of Ag in the pyrite showed a trend of gradual increase, whereas those of Mo and Au showed a tendency to first increase and then decline.

4.3.2 Chalcopyrite

Twenty-three spot analyses were conducted on the granular chalcopyrite selected from different depths within the core (Supplementary Table S2). The element with the highest concentration was Zn (avg. 840 ppm). The average contents of Ag (avg. 149 ppm, up to 258 ppm) and Cd (avg. 129 ppm, up to 2,055 ppm) were in the range 100–1000 ppm. The average contents of Ga, Ge, As, Se, In, Sb, and Pb were in the range 10–100 ppm. The Pb content was mostly low, ranging from below the detection limit to 74.1 ppm, however, some individual points showed that Pb enrichments to 172 and 698 ppm. The average contents of Ti, Cr, Mn, Co, Mo, Sn, and W were in the range 1–10. The average contents of V, Ni, Te, Ba, Au, Tl, and Bi were all <1 ppm (Table 2).

4.3.3 Sphalerite

Thirty-six sphalerite grains (including 4 colloform sphalerite and 32 massive sphalerite) were analyzed to identity the trace elements (Supplementary Table S3, Table 2). Elements with the highest concentrations were Cu (avg. 5,494 ppm) and Fe (24,461 ppm). Additionally, sphalerite was highly enriched in Cd (avg. 2,961 ppm, up to 13,272 ppm) and Pb (avg. 1,221 ppm, up to 13,272 ppm). The average contents of Ga (avg. 303 ppm, up to 1317 ppm), Ge (avg. 201 ppm, up to 596 ppm), As (avg.162 ppm, up to 890 ppm), Ag (avg. 219 ppm, up to 1044 ppm), Sb (avg. 241 ppm, up to 1006 ppm) were in the range 100–1000 ppm. The average contents of Mn and Co were in the range 10–100 ppm, and the average contents of Se, Mo, and In were in the range 1–10 ppm. The average contents of V, Cr, Ni, Sn, Te, Ba, W, Au, Tl, and Bi were all <1 ppm. Compared with pyrite and chalcopyrite, sphalerite was found more enriched in Ga, Ge, Cd, Ag, Sb, and Pb (Table 2).

4.4 *U-Th isotope ratios and U-Th ages*

The U–Th isotope systematics of the samples are presented in Table 3. The U concentrations ranged from 237 to 1871 ppb, with an average of 723.9 ppb. The Th concentrations ranged from 300 to 5795 ppt, with an average of 1732.4 ppt. The U content was extremely high in 186cm layer of the core (1841 ± 4.2 ppb). The measured $\delta^{234}U$ values ranged between 86.6 ± 2.0 and 142.4 ± 2.4 and the corrected $\delta^{234}U_{initial}$ ranged between 108 ± 3 and 144 ± 2 (Table 3). The formation age of the whole core was found to be relatively young. The corrected ^{230}Th age varied from 2297 ± 52 to 4552 ± 60 yrs. The metallogenic age of the core exhibited a trend of gradual increase from the surface to the bottom (Figure 6A). The age distribution bar chart is presented in Figure 6B.

5 Discussion

5.1 Paragenesis and spatial variation of mineralization

The microscope observations and mineralization zonation sequence of the core revealed substantial differences in the

TABLE 1 Bulk chemistry of sulfide drilling samples from the DHF.

Elements	Fe	Cu	Zn	S	Pb	Co	Ag	As	Cd	Mo	Mn	Sb	Ni	Se	Tl	V	Ga	Hg
Unit	%	%	%	%	ppm	ppm	ppm	ppm	ppm	ppm	ppm	ppm	ppm	ppm	ppm	ppm	ppm	ppm
Detection limit	0.01	0.01	0.01	0.01	0.02	0.01	0.004	0.01	0.01	0.01	0.01	0.04	0.01	0.05	0.1	0.01	0.05	0.02
Sample depth (cmbsf)																		
115	32.52	0.31	4.50	36.21	197.51	69.50	1.83	296.27	168.25	120.70	102.41	21.95	7.32	–	73.15	7.32	25.60	7.32
116	25.31	0.15	7.66	27.76	134.49	134.49	–	259.37	393.85	57.64	62.44	33.62	9.61	–	48.03	–	62.44	–
126	23.53	0.11	16.29	25.70	145.83	40.23	–	226.28	502.85	45.26	50.28	35.20	–	–	50.28	–	30.17	10.06
135	28.21	1.29	1.02	31.95	170.40	85.20	29.35	402.34	28.40	52.07	42.60	–	4.73	33.13	47.33	23.67	–	–
141	27.26	8.69	0.47	29.30	142.45	213.68	2.85	218.42	33.24	71.23	33.24	–	14.25	28.49	–	47.48	–	–
150	25.22	5.03	0.61	28.03	163.64	155.24	2.94	151.05	25.17	142.66	25.17	20.98	12.59	25.17	–	58.74	–	–
158	30.52	1.34	0.95	34.47	170.02	21.25	5.95	573.82	29.75	72.26	51.01	17.00	8.50	–	42.50	46.76	–	–
166	21.40	0.93	2.26	25.82	259.12	76.78	27.35	148.75	62.38	47.98	124.76	–	4.80	–	95.97	4.80	–	–
181	19.31	0.79	3.01	22.02	191.83	66.72	5.84	150.13	112.59	37.53	100.08	–	8.34	20.85	83.40	4.17	–	–
186	20.25	2.75	19.54	22.05	218.15	–	–	360.42	920.01	161.24	37.94	85.36	4.74	–	–	61.65	109.07	9.48
191	22.28	3.96	8.38	24.58	221.35	–	–	273.16	390.89	127.16	42.39	37.68	4.71	–	–	47.10	61.22	9.42
196	23.45	0.61	1.28	26.32	287.17	52.65	42.12	229.74	47.86	38.29	110.08	23.93	9.57	43.08	47.86	14.36	–	–
199	41.75	0.34	1.29	46.57	755.24	41.96	50.35	797.20	41.96	62.94	62.94	–	–	–	–	–	–	–

cmbsf. cm below seafloor.

10.3389/fmars.2024.1538022

10.3389/fmars.2024.1538022

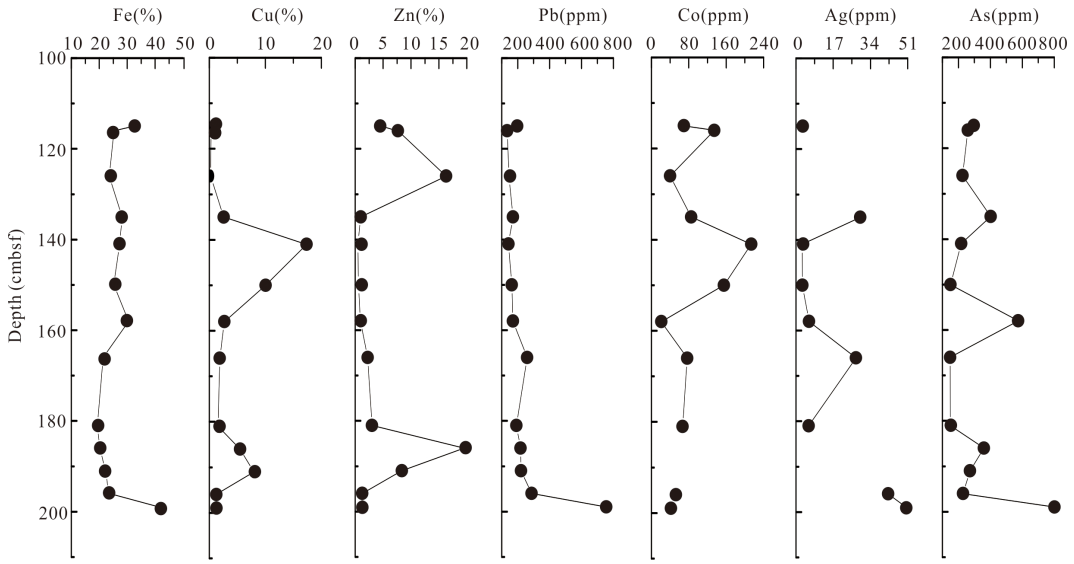

FIGURE 4
The element contents distribution of the drill core of 43-MDD07 (cmbsf: below seafloor).

TABLE 2 Summary of LA-ICP-MS data (in ppm) for samples in this study.

All data in ppm	Ti	V	Cr	Mn	Fe	Co	Ni	Cu	Zn	Ga	Ge	As	Se
Pyrite													
Minimum	0.001	0.118	0.013	0.074	na	0.090	0.005	11.6	0.799	0.001	0.767	6.22	0.002
Maximum	10.4	28.5	23.4	1027	na	1670	15.4	10814	25302	257	376	3998	144
N	141	144	123	143	na	143	140	139	141	142	144	144	144
Mean	0.932	3.67	1.89	94.4	na	151	3.30	1237	4486	4.89	8.615	417	9.71
Median	0.621	1.75	1.07	63.0	na	42.6	2.87	649	2309	0.71	3.574	257	1.45
Chalcopyrite													
Minimum	0.114	0.019	0.087	0.162	na	1.981	0.128	na	71.4	0.133	0.071	0.375	5.01
Maximum	24.1	0.686	4.61	16.5	na	53.588	2.929	na	5857	363.446	118.487	296.014	111
N	19	19	14	19		23	13		20	23	22	17	23
Mean	2.43	0.167	2.18	2.77	na	8.823	0.669	na	840	27.597	13.741	48.476	37.2
Median	1.20	0.141	1.87	1.184	na	7.104	0.425	na	146	2.631	2.394	13.535	30.1
Sphalerite													
Minimum	0.017	0.002	0.047	3.39	3598	0.003	0.004	192	na	0.002	5.86	2.71	0.014
Maximum	1.40	0.687	1.518	140	131063	294	0.707	57202	na	1317	569	890	7.23
N	35	33	21	36	36	31	25	36		36	36	36	36
Mean	0.548	0.106	0.528	31.8	24461	22.7	0.148	5494	na	304	201	162	1.85
Median	0.497	0.859	0.480	17.4	10168	0.201	0.079	3126	na	133	171	73.9	1.53
	Mo	Ag	Cd	In	Sn	Sb	Te	Ba	W	Au	Tl	Bi	Pb
Pyrite													
Minimum	0.231	0.008	0.006	0.001	0.006	0.045	0.005	0.003	0.002	0.004	0.001	0.001	0.049

(Continued)

10.3389/fmars.2024.1538022

TABLE 2 Continued

All data in ppm	Ti	V	Cr	Mn	Fe	Co	Ni	Cu	Zn	Ga	Ge	As	Se
Pyrite													
Maximum	572	474	1283	38.9	24.4	121	0.437	12.4	9.77	4.60	884	0.253	6862
N	144	144	138	136	128	143	73	131	141	136	134	81	144
Mean	64.1	91.3	34.3	1.25	1.31	14.9	0.102	0.373	0.607	0.572	98.2	0.010	992
Median	57.1	51.0	5.956	0.09	0.314	4.36	0.082	0.126	0.233	0.222	60.7	0.004	657
Chalcopyrite													
Minimum	0.001	30.9	0.256	5.16	0.815	0.001	0.127	0.014	0.027	0.001	0.009	0.001	0.007
Maximum	29.0	258	2055	53.5	20.7	116	0.969	1.00	16.6	0.128	2.94	0.116	689
N	20	23	23	23	23	18	9	13	21	18	14	15	20
Mean	2.46	149	129	16.6	5.84	13.1	0.520	0.31	1.21	0.052	0.39	0.023	58.0
Median	0.516	147	1.334	11.4	4.01	1.30	0.503	0.148	0.206	0.042	0.061	0.020	11.1
Sphalerite													
Minimum	0.005	12.3	152	0.001	0.056	1.55	0.016	0.004	0.004	0.008	0.003	0.001	26.5
Maximum	16.2	1044	13272	19.4	3.56	1007	0.999	0.351	1.58	1.52	14.0	0.051	5918
N	32	36	36	33	33	36	20	27	34	32	34	25	36
Mean	1.45	220	2961	1.76	0.701	241	0.120	0.059	0.149	0.197	0.689	0.009	1221
Median	0.132	138	2700	0.052	0.263	179	0.079	0.023	0.047	0.061	0.043	0.004	607

'na' indicates data is not applicable. Data are in ppm.

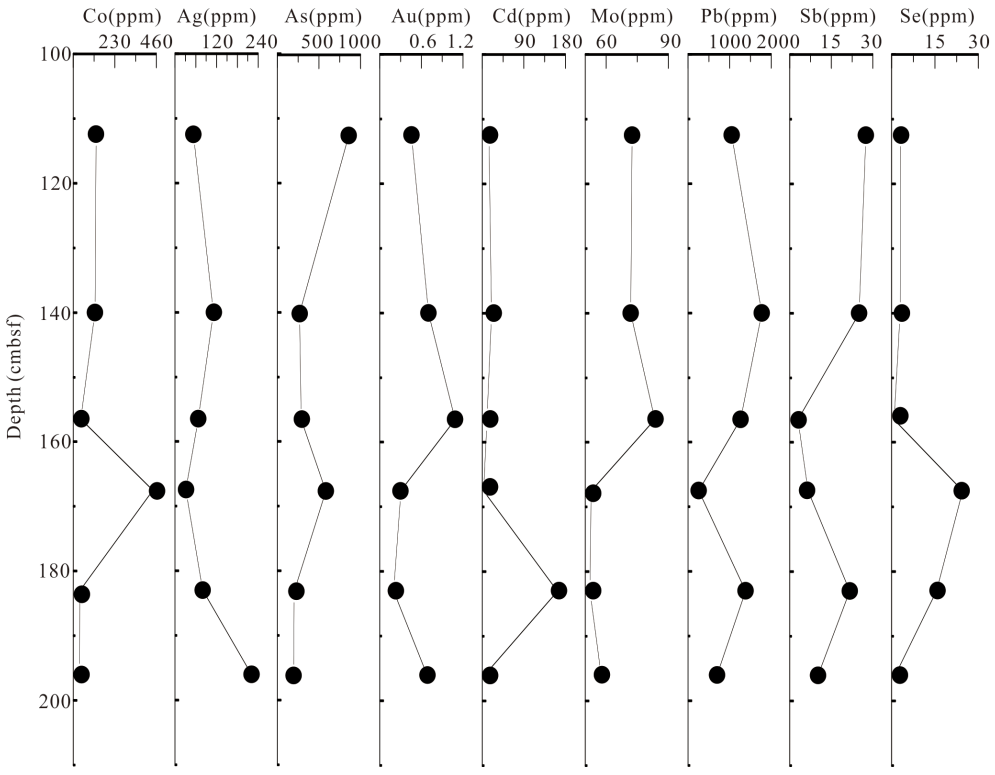

FIGURE 5
Downhole plots of the average concentrations of selected trace elements in all types of pyrite from the core.

10.3389/fmars.2024.1538022

TABLE 3 U and Th and ^{230}Th ages for sulfide drilling samples from the DHF.

Sample Number	^{238}U (ppb)		^{232}Th (ppt)		^{230}Th/^{232}Th (atomic x10^{-6})		d^{234}U* (measured)		^{230}Th/^{238}U (activity)		^{230}Th Age (yr) (uncorrected)		^{230}Th Age (yr) (corrected)		d$^{234}U_{initial}$** (corrected)		^{230}Th Age (yr BP)*** (corrected)	
115	237.0	± 0.0	1253	± 25	91.0	± 2.9	120.7	± 2.0	0.0315	± 0.0007	3104	± 70	2967	± 120	122	± 2	2949	± 120
126	375.0	± 0.5	300	± 6	485.8	± 14.6	109.9	± 2.1	0.0235	± 0.0005	2337	± 50	2316	± 52	111	± 2	2297	± 52
135	517.0	± 0.8	419	± 9	482.6	± 12.9	112.3	± 2.0	0.0237	± 0.0004	2350	± 40	2328	± 43	113	± 2	2309	± 43
150	272.8	± 0.3	733	± 15	204.0	± 7.5	106.7	± 2.4	0.0332	± 0.0010	3325	± 103	3254	± 114	108	± 2	3235	± 114
158	407	± 1	2148	± 43	115.0	± 5.0	106.6	± 4.3	0.0368	± 0.0014	3683	± 150	3545	± 179	108	± 4	3525	± 179
186	1871.0	± 4.2	5795	± 117	254.1	± 5.2	142.4	± 2.1	0.0477	± 0.0002	4650	± 23	4571	± 60	144	± 2	4552	± 60
196	1388	± 2	1479	± 30	405.5	± 11.0	109.3	± 2.1	0.0262	± 0.0005	2606	± 48	2578	± 52	110	± 2	2558	± 52
GBW04412	10278	± 14	5821	± 117	31226.7	± 631.2	852.4	± 2.2	1.0726	± 0.0021	87046	± 294	87038	± 294	1090	± 3	87017	± 294

*$\delta^{234}U = ([^{234}U/^{238}U]_{activity} - 1) \times 1000$. **$\delta^{234}U_{initial}$ was calculated based on ^{230}Th age (T), i.e., $\delta^{234}U_{initial} = \delta 234U_{measured} \times e^{\lambda 234 \times T}$. Corrected ^{230}Th ages assume the initial $^{230}Th/^{232}Th$ atomic ratio of 4.4 ±2.2 ×10-6. Those are the values for a material at secular equilibrium, with the bulk earth $^{232}Th/^{238}U$ value of 3.8. The errors are arbitrarily assumed to be 50%.
***B.P. stands for "Before Present" where the "Present" is defined as the year 2000 A.D.

mineralization features between the upper, middle, and bottom parts of the core (Figure 7). The upper part of the core (layer I) is dominated by granular pyrite, containing a small amount of colloform pyrite and late granular pyrite. The central part of the core (layer III) is dominated by euhedral pyrite, although the lower part is dominated by granular pyrite. The bottom of the core (layer V) is dominated by colloform pyrite. The marcasite content is relatively high, whereas the sphalerite content is low at the bottom of the core (layer V). The following paragenetic associations are apparent through the core: chalcopyrite + euhedral pyrite (Py4) → chalcopyrite + granular pyrite (Py1) + massive sphalerite (Sp1) → marcasite + coarse-grained pyrite (Py2) + massive sphalerite (Sp1) → later recrystallized pyrite (Py2) + colloform sphalerite (Sp2) → colloform pyrite (Py3) + marcasite → amorphous silica. Compared with the lower-middle part of the core, the upper-middle part of the core is notably enriched copper-rich minerals such as chalcopyrite, which might suggest a sustained influence by high-temperature hydrothermal activity (Hannington et al., 1995).

In the early stage, large quantities of high-temperature minerals formed, which included chalcopyrite and associated euhedral pyrite and euhedral sphalerite. The second stage and the low-temperature stage comprised the main ore-forming period of the core, when a large quantity of massive pyrite formed. The late stage is characterized by silicification caused by cooling of the hydrothermal fluids, resulting in precipitation of high quantities of amorphous silica.

5.2 Controlling factors on trace elements

5.2.1 Controls on trace elements in pyrite

Time-resolved LA-ICP-MS analytical signals revealed a uniform distribution of most elements such as Pb, Zn, Cu, Co, As, Sb, Mo, and Ag (Figures 8A, B) in the granular and colloform pyrite, indicating that these elements are present mainly in lattice substitutions rather than as inclusions of other sulfides. However, in the euhedral pyrite, the distribution trend of Cu revealed by the analytical signals was different from that of most other elements, suggesting that chalcopyrite inclusions might be present (Figure 8C).

Pyrite is widely distributed within hydrothermal deposits (Cook et al., 2009; Deditius et al., 2014; Keith et al., 2016a); it is the most common sulfide phase in seafloor massive sulfides and its precipitation can effectively control the distribution of many trace elements (Hannington, 2014; Keith et al., 2016a; Large et al., 2009; Maslennikov et al., 2009).Previous studies suggested that pyrites have crystallized at low temperatures are rich in Pb, As, Mn, Tl, Ag and Cd (Metz and Trefry, 2000; Maslennikov et al., 2009). Pyrites have crystallized at high temperatures are rich in Co, Se, Sn and Ni (Keith et al., 2016a; Maslennikov et al., 2009; Meng et al., 2020). Pyrite in the studied core is characterized by high contents of Mn, Co, As, Mo, Ag, Cd, Sb, Tl and Pb, and low contents of Ti, Ga, In, Sn, Ni, Se, Ba, W and Au (Table 2). This might suggest that the formation of the sulfide mound underwent a combined process of low-temperature and high-temperature mineralization.

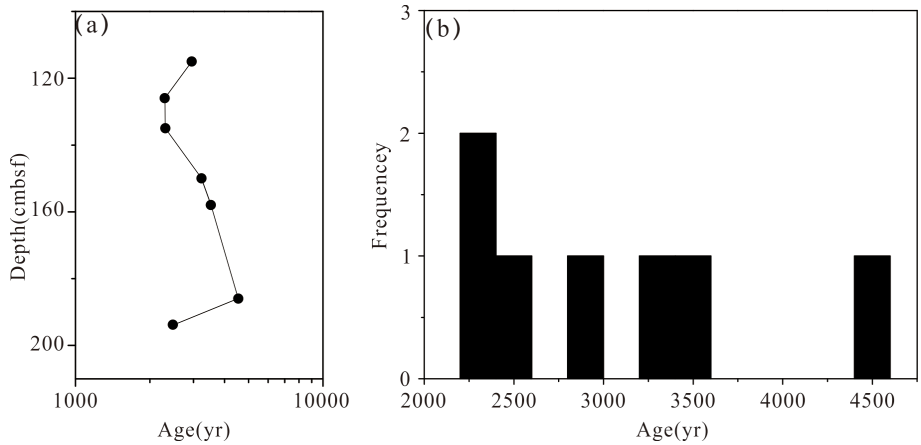

FIGURE 6
Age distribution of hydrothermal sulfide samples from the DHF, **(A)** The age distribution of the drill core of 43-MDD07 (cmbsf: below seafloor) **(B)** Age error bar chart frequency-age diagram.

The source of the relatively enriched As in pyrite is primarily the hydrothermal fluids, and a low-temperature environment is favorable for its occurrence (Huston et al., 1995; Metz and Trefry, 2000; Maslennikov et al., 2009; Wohlgemuth-Ueberwasser et al., 2015). The As contents in the granular pyrites in layer I are higher than other layers and there are no significant differences in As content among the pyrite types. The positive correlation found between As and Sb in the pyrite is possibly because metals such As and Sb are derived via sphalerite reactivation and might be influenced by zonal refining (Keith et al., 2016a). Thus, zone refining was likely a key factor controlling As and Sb behavior. At medium–high temperatures and in a reducing hydrothermal fluid, Mn has high solubility (Large et al., 2007; Maslennikov et al., 2009; Grant et al., 2018), the high concentrations of Mn in the granular pyrite of layer IV might reflect low fluid temperature and a relatively oxidized seawater environment. Although the low-temperature mineral galena was not detected in the DHF, the highest Pb content observed in granular pyrite replaced by sphalerite suggests the potential presence of Pb-mineral inclusions (Figure 8; Smith and Huston, 1992). This is because Pb is unlikely to substitute directly into the sulfide lattice due to its large ionic radius (George et al., 2018; Grant et al., 2018).

The range of concentration of Tl is large (0.001–884 ppm) with the maximum content found in the granular pyrite of the bottom layer of the core (Supplementary Table S1). Usually, Tl is preferentially enriched in sulfide under low-temperature conditions (approximately 100–250°C) and it has high solubility in high-temperature hydrothermal fluids (Huston et al., 1995; Wang et al., 2017; Maslennikov et al., 2009). Mo is mainly derived from seawater and its solubility in high-temperature fluid decreases sharply (Von Damm, 1995; Douville et al., 2002; Metz and Trefry, 2000). The solubility of Mo derived mainly from seawater is markedly reduced in a high-temperature fluid (Keith et al., 2016a). The range of concentration of Mo is very wide with the maximum content (572ppm) found in the granular pyrite in layer I (Supplementary Table S1) which suggests that this layer is formed under strong hydrothermal-fluid-seawater mixing conditions.

The Ag content is enriched in the colloform pyrite at the bottom of the core, whereas it is relatively low in the euhedral pyrite (Supplementary Table S1). The distribution of Ag might be related to seawater–hydrothermal fluid mixing front as Ag solubility decreases with increasing pH and decreasing temperature (Butler and Nesbitt, 1999; Wang et al., 2017). The Ni contents are very low in all types of pyrite. The depletion of Ni may also reflect the influence of fluid-seawater mixing (i.e., sub-seafloor mixing) (Gini et al., 2024). Consequently, the pronounced variation in the concentrations of Pb, Tl, Mn, As, Se, Ag, Sb, and Ni in pyrite throughout the core indicates that seawater mixing may have played a crucial role in fluctuating the physicochemical conditions of the hydrothermal fluid during the mineralization process.

5.2.2 Controls on trace elements in chalcopyrite

The ablation profiles of Cr, Mn, Co, Zn, Ge, As, Se, In, Sn, and Pb were relatively uniform (Figure 8D), indicating that these elements are present mainly as substitutions in the mineral lattice (e.g., In for Cu; Co and Sn for Fe, Huston et al., 1995). The ablation profile of Ag was different from that of other elements, and the appearance of sharp peaks might indicate that the effect of mineral inclusions containing the element of Ag (Huston et al., 1995; Grant et al., 2015; George et al., 2016).

Previous studies revealed that chalcopyrite is generally a relatively poor carrier of trace elements (Cook et al., 2011; George et al., 2016; Keith et al., 2016b). Compared with the contents of Sb, Co, Au, and Sn in chalcopyrite, those of Ag, Pb, Cd, and Se are relatively high. The Au content exhibits no correlations with Ag, Pb and Sb (Figures 9A–C). Typically, Au is common in medium-temperature associations, whereas Pb is common in lower-temperature associations (Halbach et al., 2003). The precipitation of Ag in chalcopyrite is sensitive to increasing pH (Tivey et al., 1999), and lower-temperature and stronger oxidation conditions

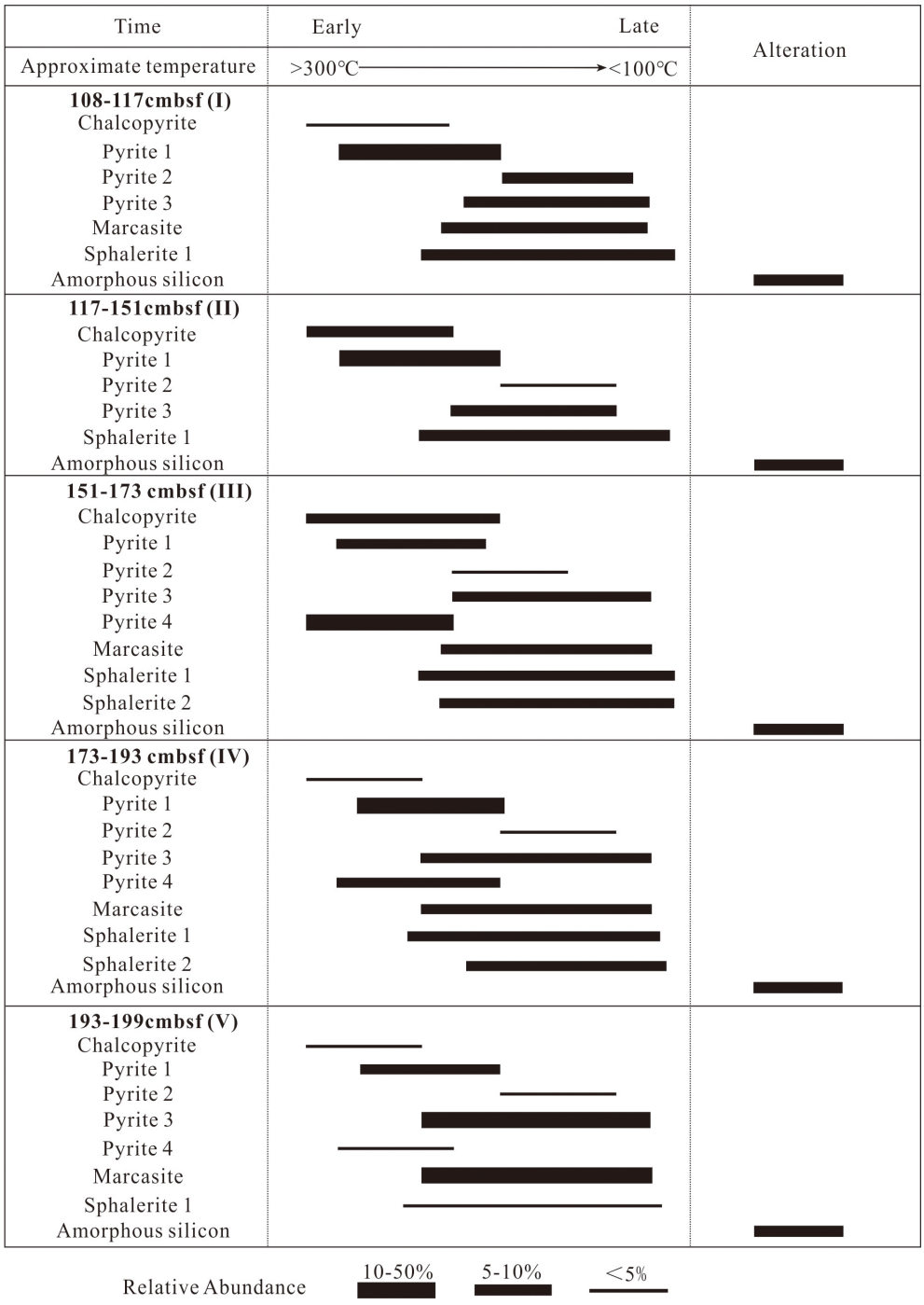

FIGURE 7
Paragenetic sequences of mineralization in sulfides from the DHF.

are conducive to Ag precipitation in micro- inclusions; conversely, high-temperature reducing conditions are conducive to Ag entering chalcopyrite in the form of lattice substitution (Huston et al., 1995; Grant et al., 2015).

The maximum content of Zn in the chalcopyrite reached 0.33 wt.%, and no Zn-bearing inclusions were observed (Shalaby et al., 2004; Helmy et al., 2014). Therefore, we conclude that Zn in the chalcopyrite exists mainly in solid solution. This is supported by the fact that Cd, a typical element in sphalerite, shows a positive correlation with Zn (Figure 9D). Meanwhile, Co and Se are indicators of fluid with high temperatures (Herzig et al., 1998; Grant et al., 2018). The Co contents are much lower than the average contents of seafloor sulfides (236 ppm, Hannington et al., 2005) and ferromanganese nodules on their surfaces (Ren et al., 2022, Ren et al., 2024). The Se content has no correlation with both Co and Sn (Figures 9E, F). Previous studies suggested that the content of Se can be controlled by the temperature of precipitation, with Se-rich and Se-poor chalcopyrite precipitating at high and

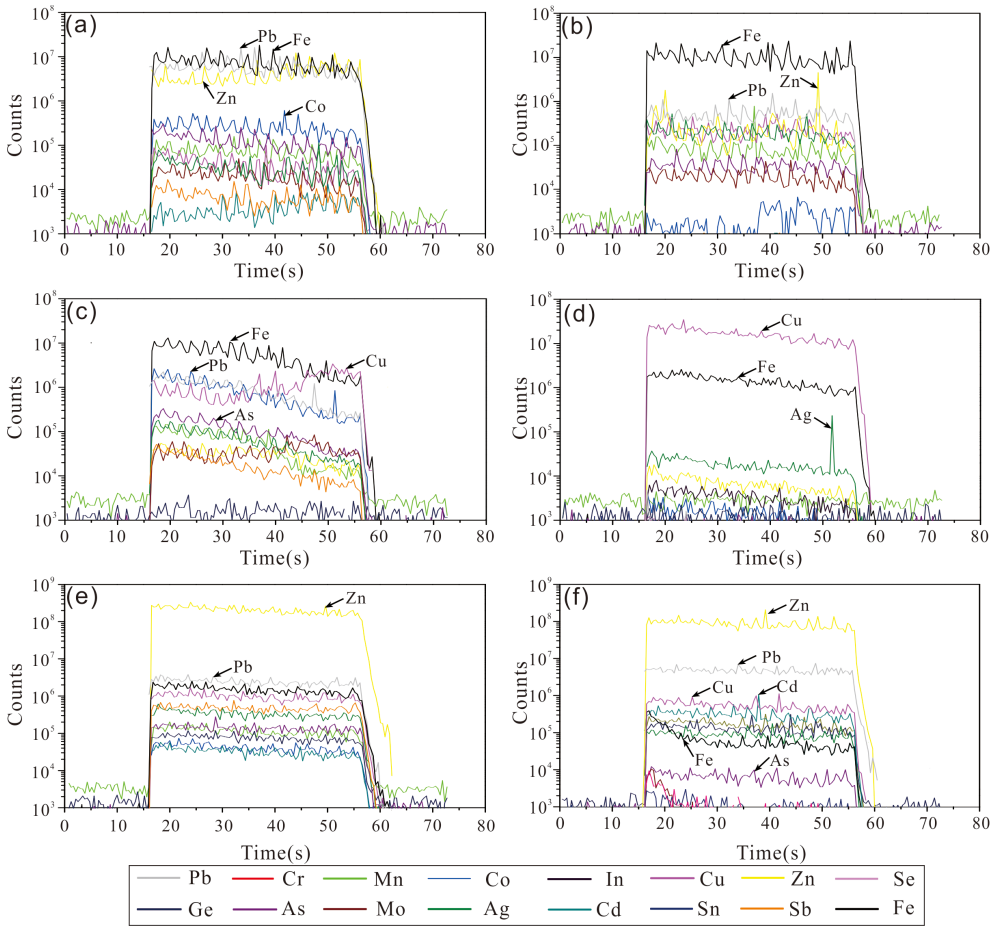

FIGURE 8
Examples of LA-ICP-MS profiles (time-resolved) for sulfides in the DHF field. **(A)** Ablation profile for granular Py of 129-151cmbsf; **(B)** Ablation profile for colloform Py of 193-199cmbsf; **(C)** Ablation profile for euhedral Py replaced by Ccp of 162-173 cmbsf; **(D)** Ablation profile for granular Ccp of 162-173 cmbsf; **(E)** Ablation profile for grained Sph of 151-162 cmbsf; **(F)** Ablation profile for colloform Sph of 108-117 cmbsf. Mineral abbreviations: Py, pyrite; Ccp, chalcopyrite; Sp, sphalerite.

medium-low temperatures, respectively (Auclair et al., 1987; Rouxel et al., 2004). The wide range of Se contents (5.81–112 ppm) can be interpreted as reflecting variable degrees of fluid-seawater mixing. Owing to the structure of stannite (Cu_2FeSnS_4) being very similar to that of $CuFeS_2$, chalcopyrite can incorporate Sn at high temperatures (300–500°C) (Maslennikov et al., 2009). The chalcopyrite in our study area has a relatively low Sn content which indicate that a complex mineralization process indeed occurred.

5.2.3 Controls on trace elements in sphalerite

The ablation profiles of Pb, Ag, Sb, Mn, Co, and Cd in both the granular and the colloform sphalerite were relatively smooth, indicating that these elements might occur as lattice substitution in minerals (Figures 8E, F). Lack of correlation between Fe and Cu indicated that submicroscopic chalcopyrite inclusions were not involved in the analyses. However, Pb, Ag, Ga, and Sn in the colloform sphalerite occasionally exhibited irregular undulating spectral lines, suggesting that these elements might be present as nanoscale inclusions (Figure 8F).

The concentrations of Cd, Pb, Ag, Cr, Mn, As, Sn, Ga, and Ge in sphalerite are higher than those in pyrite and chalcopyrite. Sphalerite precipitates under a range of temperature, pressure, sulfur fugacity, and oxygen fugacity conditions (e.g., Keith et al., 2014). When the ore-forming fluid is at or below 250 °C, Zn is preferentially precipitated in the form of sphalerite (Metz and Trefry, 2000; Hannington et al., 2005; Hannington, 2014). A high concentration of Pb (avg. 1,221 ppm) was found in all samples of sphalerite, likely indicating the presence of Pb-bearing mineral inclusions formed under medium–low temperature and moderately reducing conditions (Grant et al., 2018). Positive correlation (coefficient of determination R^2 = 0.73) between As and Pb can best be interpreted in terms of nanoscale inclusions of galena or sulfosalts (Figure 10A).

High Cd concentrations (up to 13,272 ppm) are also found in all the studied samples. The most common mineral of Cd is sphalerite, and the high concentrations of Cd are caused by the replacement of Cd^{2+} for Zn^{2+} (Cook et al., 2009). Variations in the Cd and Sn contents of sphalerite might reflect fluctuating fluid chemistry and deposition temperature (Scott and Barnes, 1972). In high-

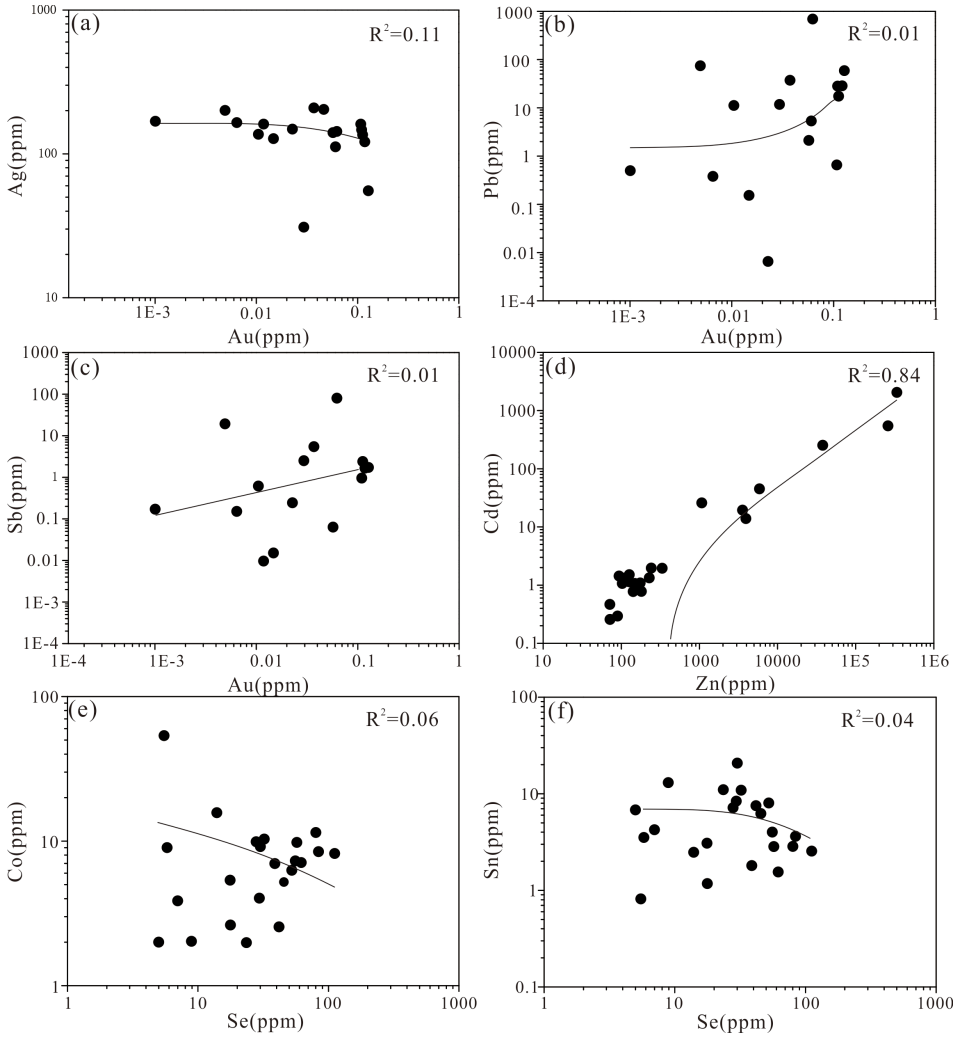

FIGURE 9
Correlation plots of **(A)** Au-Ag; **(B)** Au-Pb; **(C)** Au-Sb; **(D)** Zn-Cd; **(E)** Se-Co; **(F)** Se-Sn in chalcopyrite from the DHF.

temperature, acidic, reducing hydrothermal solutions, Sn can be transported as the Sn(II) aqueous complex, such as $SnCl_2$ (Heinrich and Eadington, 1986). Given the low Sn content and its lack of correlation with Cd in this study, the substitution of Sn^{2+} for Zn^{2+} in ZnS can be expected (Figure 10B; Maslennikov et al., 2009).

The high Ag concentration in sphalerite might be caused by periodic reduction in temperature and rapid precipitation of Ag from the original high temperature, strongly reducing fluid (Maslennikov et al., 2009). The sphalerite samples contain high concentrations of Sb (up to 1,006 ppm). The weak correlation between Ag and Sb (R^2 = 0.23) (Figure 10C) suggests a limited degree of $2Zn^{2+} \leftrightarrow Ag^{+} + Sb^{3+}$ substitution and the inclusion of Ag—Sb bearing minerals (Cook et al., 2009). These trace elements commonly precipitate under lower temperature conditions. All the samples show enrichment in Ga and Ge but there is no evident correlation between Ga and Ge (Figure 10D). The transport of Ga in sphalerite is dominated by neutral to weakly charged hydroxyl complexes, even in a hydrothermal solution containing reduced sulfur (Wood and Samson, 2006). Consequently, the high contents of Ga and Ge in the sphalerite might explained by coupled substitution rather than direct substitution for Zn (II) (Cook et al., 2009).

5.3 Distribution of trace elements in pyrite with depth below the seafloor

The distribution of ages within the surface of the DHF sulfide mound indicates a complex evolution process. The relatively intense hydrothermal activity over the past 4,552 years can be broadly divided into five different mineralization periods: 2,949 years (108–117 cmbsf), 2,307–2,297 years (117–151 cmbsf), 3,523–3,253 years (151–173 cmbsf), 4,552 years (173–193 cmbsf), and 2,558 years (193–199 cmbsf) (Table 3, Figure 6A). Apart from the top and the bottom, the core has obvious characteristics of gradual accumulation of mineralization. At the bottom and top, it is considered that hydrothermal seepage and metasomatic mineralization occurred continuously in the interior of the mound.

The distributions of Co, Ag, As, Au, Cd, Mo, Pb, Sb, and Se in the pyrite with depth below the seafloor are shown in Figures 11A–I.

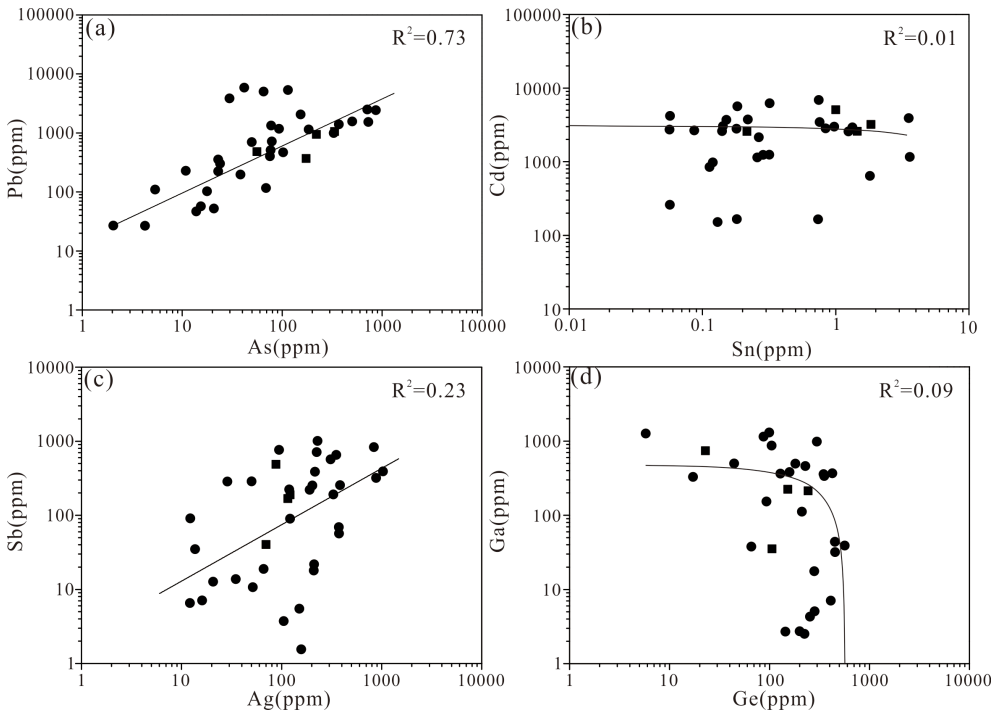

FIGURE 10
Correlation plots of **(A)** As vs. Pb, **(B)** Sn vs. Cd, **(C)** Ag vs. Sb, and **(D)** Ga vs. Ge in sphalerite from DHF. The dots and the boxes represent the grained sphalerite and colloform sphalerite respectively.

Pyrite in the DHF is generally enriched in Pb, As, Ag, Cd, Mo, and Sb and relatively depleted in Co, Se, and Au. The Se content is relatively low in most of the pyrites except the euhedral pyrites in the central part of the core. The As content of the granular pyrite was higher than that of the colloform pyrite, which might reflect direct precipitation from As-rich hydrothermal fluids (Huston et al., 1995; Kristall et al., 2006). The granular pyrite at layer I is enriched in Ag, As, Mo, Pb, and Sb compared with other types of pyrite at other layers. The granular pyrite and late recrystallized pyrite at layer II are enriched in Ag, Mo, Pb, and Se. The euhedral pyrite at layer III is enriched in Co, As, Se, Sb and Pb. The enrichment of Co and Se in euhedral pyrite suggests high-temperature mineralization (Metz and Trefry, 2000; Martin et al., 2023). This is in reasonable agreement with the mineralogical observations that euhedral pyrite is often associated with chalcopyrite or distributed in the inner wall of the hydrothermal channel. The granular pyrite at layer IV is enriched in Cd, Ag, Au and Pb. The colloform pyrite at layer V is enriched in Ag, Pb and depleted in Co and Se.

According to the chronological model, the shallow sulfide mound reflects a superposition process. Pyrites of different layers and different periods show obvious metasomatism. The variation in the elemental contents in different layers and types of pyrite is controlled by the evolution of physicochemical conditions of the hydrothermal fluid attributable to the interaction of seawater and hydrothermal fluids within the sulfide mound. The shallow sulfide mound underwent a mineralization process of precipitation followed by multiple metasomatic precipitation episodes over a short period. Owing to the limitations of the current domestic drilling rig used in the collection of the sulfide samples, further technological advances are required to enable deeper sulfide sampling. It is also necessary to refine the chronological evolution to the point where individual episodes can be resolved with confidence.

5.4 Comparison with trace elements in pyrites from other hydrothermal fields along the mid-ocean ridges

Compared with other hydrothermal fields along the mid-ocean ridges (e.g., Longqi, Tianzuo, and East Longjing on the SWIR, Wocan on the Northwest Indian Ridge, Edmond, Meso zone, and Kairei on the Central Indian Ridge, and TAG, 5°S and Logatchev on the Mid-Atlantic Ridge) (Yuan et al., 2018b; Liao et al., 2021; Ding et al., 2022; Wang et al., 2017; Zhang et al., 2023; Keith et al., 2016a), all types of pyrite in the DHF are generally enriched in Zn, Pb, As, Ag, Cd, Mo and Sb and relatively depleted in Co and Se (Figure 12). Pb shows positive correlations with Zn, Ag, Cd, Mo, and Sb with coefficients of determination of 0.87, 0.80, 0.79, 0.41, and 0.62, respectively (Figures 12A, C, D, F, H). Correlations between Pb and As, Pb and Co, and Pb and Se, are weak (Figures 12B, E, G). This contrasts with the enrichment of Zn, Pb, Ag, Cd, Mo, and Sb in back-arc basin deposits, which is partly attributed to the influence of felsic rocks and/or thick terrigenous sediments (Herzig et al., 1993; Keith et al., 2016a; Yeats et al., 2017). Moreover, some pyrite grains from the sediment-starved mid-ocean ridges such as 5°S and the Meso zone also show enrichment in Zn and Cd, which in some

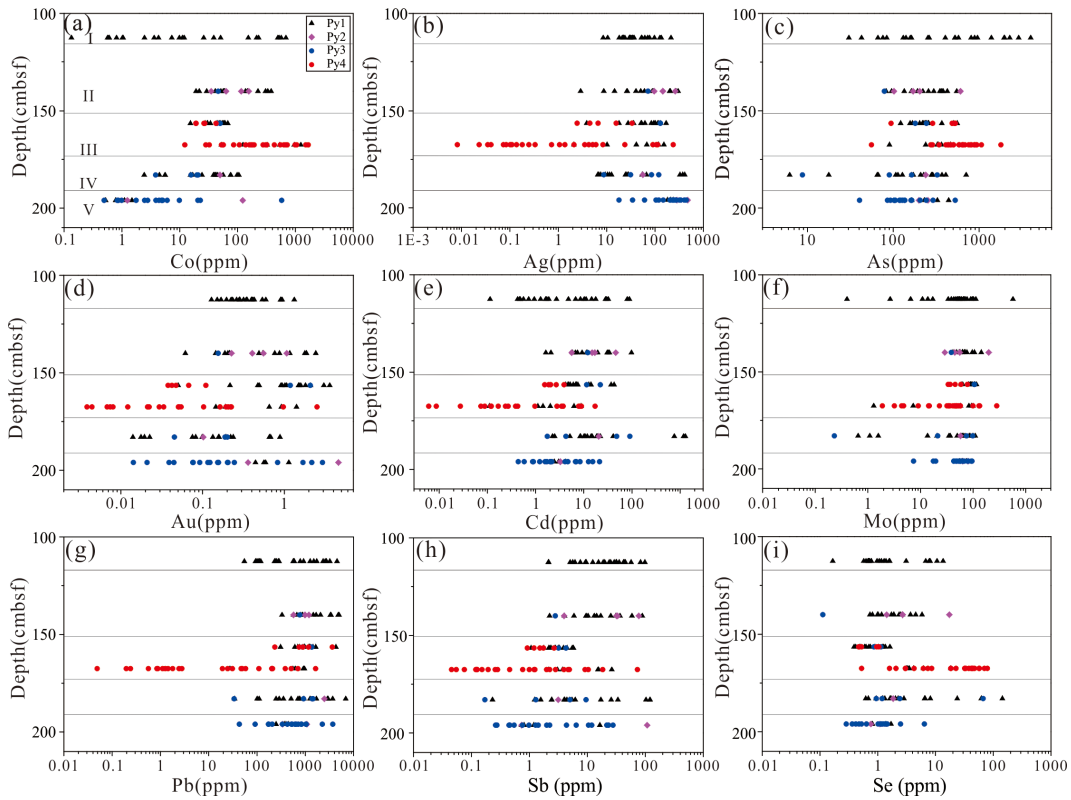

FIGURE 11
The distribution of trace elements in pyrite from different layers in the DHF. **(A–I)** represent the distribution of Co, Ag, As, Au, Cd, Mo, Pb, Sb, and Se respectively. All layers are calculated at intermediate depth. Py1: granular pyrite, Py2: late overgrowths coarse granular pyrite, Py3: colloform pyrite, Py4: euhedral pyrite. Layer I to V corresponds to 2,949 years (108–117 cmbsf), 2,307–2,297 years (117–151 cmbsf), 3,523-3253 years (151–173 cmbsf), 4,552 years (173–193 cmbsf) and 2,558 years (193–199 cmbsf) respectively.

cases might reflect the precipitation processes rather than a sediment related metal source (Keith et al., 2016a).

Previous studies suggested that fluid boiling can enhance the enrichment of As, Cu, Pb, Ag, and Au while depleting Co and Ni in pyrite from various active seafloor and continental hydrothermal systems (Román et al., 2019; Wang et al., 2022; Dang et al., 2023). This is primarily because fluid boiling significantly impacts the physicochemical conditions of hydrothermal fluids, including temperature, chloride concentration, pH, and oxygen fugacity which consequently causes abrupt alterations in the solubility and distribution of these elements (Keith et al., 2014, Keith et al., 2016a; Tivey et al., 1999). In contrast, the concentrations of As, Cu, and Pb in DHF pyrite are significantly lower compared to those precipitated in association with the aforementioned fluid boiling (Table 2; Román et al., 2019; Wang et al., 2022; Dang et al., 2023). This can be attributed to the absence of fluid boiling in DHF, as confirmed by results from phase-separation simulations conducted using the salt-water ($NaCl$-H_2O) Equation of State software (https://www.xthermal.info/en/index.html).

The enrichment of As, Sb, Ag, Pb and lower contents of Co and Se in the pyrite of the Brothers hydrothermal system can be explained by seawater mixing during shallow recharge (Martin et al., 2023). Additionally, these elements have the common characteristic that they tend to precipitate at low temperatures; consequently, the unique mineralization process of particular deposits might play an important role in the enrichment of such elements. Bulk geochemical results of massive sulfide collected by TV grabs in this area showed that these sulfides have high contents of Pb, As, Cd, and Ag. Because of the frequent magma activities, extremely low spreading rate at the DHF, long duration hydrothermal activity, multi-stage mineralization, early precipitated Ag, Sb, Pb, As and Cd in subseafloor sulfide would be remobilized in the following episode of hydrothermal activity (Yang et al., 2023). The bulk chemistry of the core analyzed in this study exhibits the same feature. Therefore, the DHF, as a typical axial volcanic ridge sediment-starved hydrothermal field, exhibits trace element compositions that have obvious particularity compared with other mid-ocean ridge hydrothermal fields. This is further supported by multistage mineralization, as evidenced by varying ages determined through ^{230}Th/U dating (Figure 6). The chalcopyrite and sphalerite in the DHF are also enriched in As, Sb, Ag, and Pb. Ascending hydrothermal fluid undergoes mixing and cooling within seawater, causing pronounced change in the fluid temperature and deposition of pyrite, chalcopyrite and sphalerite with high contents of As, Sb, Ag, and Pb. The enrichment of As, Sb, Ag, and Pb and the lower contents of Co and Se in the pyrite are best explained by shallow subsurface mixing during different periods of hydrothermal activity.

10.3389/fmars.2024.1538022

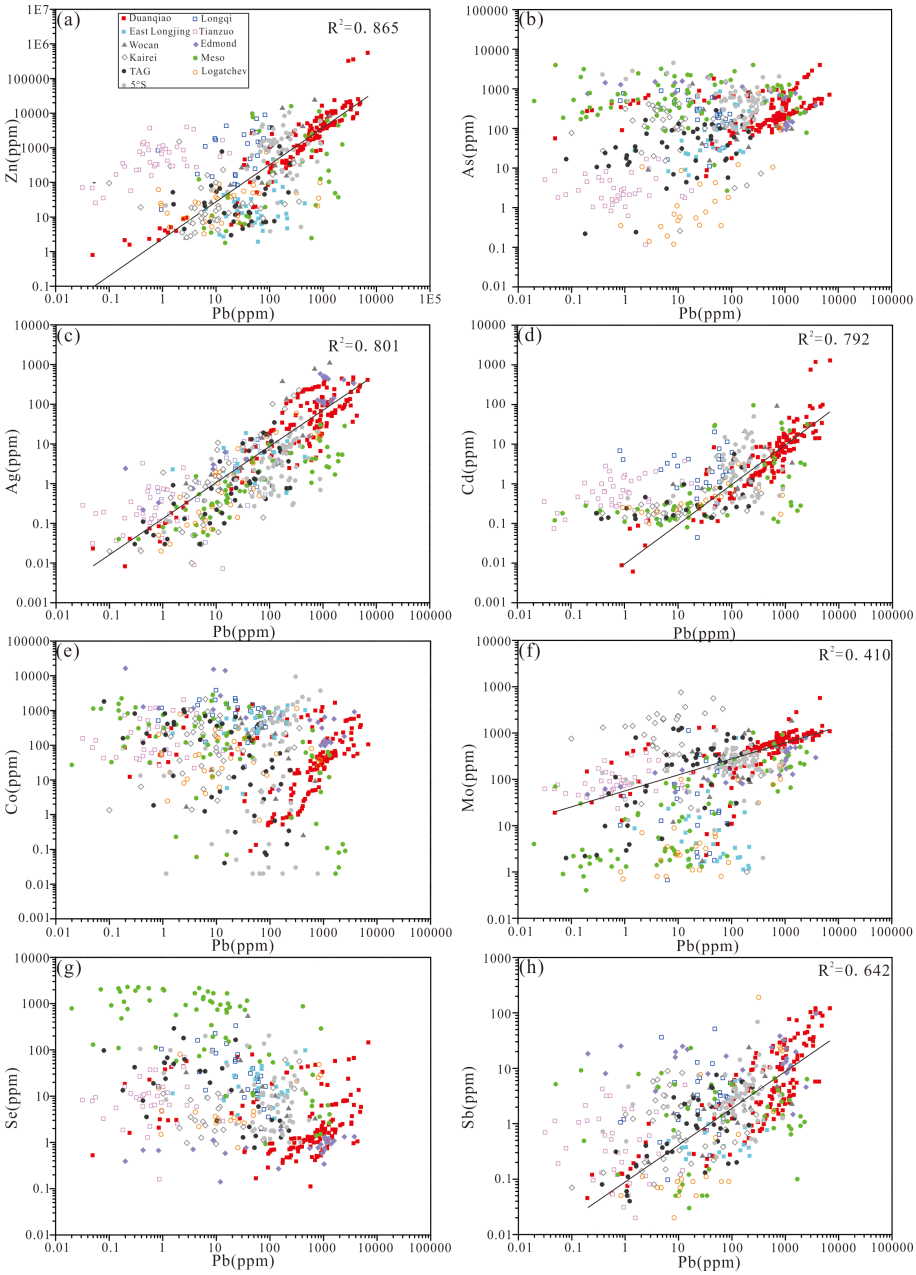

FIGURE 12
Concentrations of **(A)** Zn, **(B)** As, **(C)** Ag, **(D)** Cd, **(E)** Co, **(F)** Mo, **(G)** Se and **(H)** Sb vs. Pb in pyrite from various hydrothermal fields along the mid-ocean ridges. Longqi (Yuan et al., 2018b), East Longjing (Liao et al., 2021), Tianzuo (Ding et al., 2022), Wocan (Wang et al., 2017), Edmond (Zhang et al., 2023), Karei, Meso, TAG, Logatchev and 5°S (Keith et al., 2016a). Filled symbols and empty symbols represent the basalts-hosted and ultramafic-hosted hydrothermal fields respectively.

6 Conclusion

A sulfide drill core recovered from the DHF on the ultraslow spreading SWIR was studied in detail to understand the mineralization conditions, enrichment mechanism of metallogenic elements, and the associated evolution process. Analysis revealed that granular pyrite dominated the upper part of the core, euhedral pyrite dominated the central part of the core and colloform pyrite dominated the bottom of the core.

Pyrite is characterized by high Mn, Co, As, Mo, Ag, Cd, Sb, Tl and Pb contents, and is characterized by low Ti, Ga, In, Sn, Ni, Se, Ba, W and Au contents. Chalcopyrite is characterized by high concentrations of Se, Sn, In, As, Ag and Pb and sphalerite is characterized by high concentrations of Co, Ga, Ge, As, Ag, Cd, Sb and Pb. The ^{230}Th/U dating data suggests five different mineralization periods, and the core has obvious characteristics of gradual accumulation of mineralization during 4,552–2,297 years. The variations in the elemental contents of the different layers and the different types of pyrite were controlled by

the evolution of the physicochemical conditions of the hydrothermal fluid caused by the interaction of seawater and hydrothermal fluids within the sulfide mound.

Compared with other hydrothermal fields along other mid-ocean ridges, the pyrite in the DHF is generally enriched in Zn, Pb, As, Ag, Cd, Mo, and Sb, which might be attributed to shallow subsurface mixing during different periods of hydrothermal activity. This work provides the first documentation of the evolution process of a shallow sulfide mound on the SWIR.

Data availability statement

The original contributions presented in the study are included in the article/supplementary material. Further inquiries can be directed to the corresponding author.

Author contributions

WY: Conceptualization, Data curation, Formal analysis, Writing – original draft, Methodology. CT: Funding acquisition, Writing – review & editing, Resources. SL: Methodology, Writing – review & editing. HZ: Writing – review & editing, Data curation. CZ: Methodology, Data curation, Writing – review & editing. WL: Data curation, Writing – review & editing. GZ: Software, Writing – review & editing. XW: Methodology, Writing – review & editing. LW: Methodology, Writing – review & editing.

Funding

The author(s) declare that financial support was received for the research, authorship, and/or publication of this article. This work was supported by the National Natural Science Foundation of China (Grant No. 42127807), Natural Science Foundation of China (Grant No. 42406226), National Key Research and Development Project of China (2023YFC2811100), COMAR (China Ocean Mineral Resources R & D Association) Project (Grant No. DY135-S1-1-01, DY135-S1-1-02).

Conflict of interest

The authors declare that the research was conducted in the absence of any commercial or financial relationships that could be construed as a potential conflict of interest.

Generative AI statement

The author(s) declare that no Generative AI was used in the creation of this manuscript.

Publisher's note

All claims expressed in this article are solely those of the authors and do not necessarily represent those of their affiliated organizations, or those of the publisher, the editors and the reviewers. Any product that may be evaluated in this article, or claim that may be made by its manufacturer, is not guaranteed or endorsed by the publisher.

Supplementary material

The Supplementary Material for this article can be found online at: https://www.frontiersin.org/articles/10.3389/fmars.2024.1538022/full#supplementary-material

References

Auclair, G., Fouquet, Y., and Bohn, M. (1987). Distribution of selenium in high-temperature hydrothermal sulfide deposits at 13° North, East Pacific Rise. *Can. Mineralogist* 25, 577–5872-s2.0-0023588769

Butler, I. B., and Nesbitt, R. W. (1999). Trace element distributions in the chalcopyrite wall of a black smoker chimney: insights from laser ablation inductively coupled plasma mass spectrometry (LA–ICP–MS). *Earth Planetary Sci. Lett.* 167, 335–345. doi: 10.1016/S0012-821X(99)00038-2

Cannat, M., Rommevaux-Jestin, C., Sauter, D., Deplus, C., and Mendel, V. (1999). Formation of the axial relief at the very slow spreading Southwest Indian Ridge (49° to 69°E). *J. Geophysical Research: Solid Earth* 104, 22825–22843. doi: 10.1029/1999jb900195

Cao, H., Sun, Z. L., Jiang, Z. K., Dong, A. G., Geng, W., Zhang, X. L., et al. (2021). Source origin and ore-controlling factors of hydrothermal sulfides from the Tianzuo hydrothermal field, southwest Indian ridge. *Ore Geology Rev. 134* 8), 104168. doi: 10.1016/j.oregeorev.2021.104168

Chen, J., Cannat, M., Tao, C. H., Sauter, D., and Munschy, M. (2021). 780 thousand years of upper-Crustal construction at a melt-rich segment of the ultraslow spreading southwest Indian ridge 50°28′E. *J. Geophysical Research: Solid Earth* 126, e2021JB022152. doi: 10.1029/2021JB022152

Cheng, H., Edwards, R. L., Shen, C. C., Woodhead, J., Hellstrom, J, Wang, Y. J., et al. (2013). Improvements in 230Th dating, 230Th and 234U half-life values, and U–Th isotopic measurements by multi-collector inductively coupled plasma mass spectrometry. *Earth Planet Sci Lett.* 371–372, 82–91. doi: 10.1016/j.epsl.2013.04.006

Cherkashov, G. A., Firstova, A. V., Bich, A. S., Kuksa, K. A., Sukhanova, A. A., Yakovenko, E. S., et al. (2023). Geochronological study of hydrothermal precipitates in the northern equatorial area of the mid-atlantic ridge. *Geotectonics* 57, S69–S83. doi: 10.1134/S001685212307004X

Cherkashov, G., Kuznetsov, V., Kuksa, K., Tabuns, E., Maksimov, F., and BeĽtenev, V. (2017). Sulfide geochronology along the Northern Equatorial Mid-Atlantic Ridge. *Ore Geology Rev.* 87, 147–154. doi: 10.1016/j.oregeorev.2016.10.015

Choi, S. K., Pak, S. J., Park, J. W., Kim, H. S., Kim, J. K., and Choi, S. H. (2023). Trace –element distribution and ore–forming processes in Au-Ag–rich hydrothermal chimneys and mounds in the TA25 West vent field of the Tonga Arc. *Mineralium Deposita* 58, 135–160. doi: 10.1007/s00126-022-01136-w

Cook, N. J., Ciobanu, C. L., Danyushevsky, L. V., and Gilbert, S. (2011). Minor and trace elements in bornite and associated Cu–(Fe)-sulphides: A LA-ICP-MS study. *Geochimica Cosmochimica Acta* 75, 6473–6496. doi: 10.1016/J.GCA.2011.08.021

Cook, N. J., Ciobanu, C. L., Pring, A., Skinner, W., Shimizu, M., Danyushevsky, L., et al. (2009). Trace and minor elements in sphalerite: A LA-ICPMS study. *Geochimica Cosmochimica Acta* 73, 4761–4791. doi: 10.1016/j.gca.2009.05.045

Dang, Y., Li, C. S., Shi, X. F., Wang, S., Ye, J., Li, B., et al. (2023). Metallogenetic process of Xunmei hydrothermal field (26°S), South Mid-Atlantic Ridge: Constraints

from *in-situ* sulfur isotope and trace elements of sulfides. *Mar. Geology* 466, 107182. doi: 10.1016/j.margeo.2023.107182

Deditius, A. P., Reich, M., Kesler, S. E., Utsunomiya, S., Chryssoulis, S. L., Walshe, J., et al. (2014). The coupled geochemistry of Au and As in pyrite from hydrothermal ore deposits. *Geochimica Cosmochimica Acta* 140, 644–670. doi: 10.1016/j.gca.2014.05.045

Dick, H. J. B., Lin, J., and Schouten, H. (2003). An ultraslow-spreading class of ocean ridge. *Nature* 426, 405–412. doi: 10.1038/nature02128

Ding, T., Wang, J., Tao, C. H., Dias, Á.A., Liang, J., Wang, Y., et al. (2022). Trace-element compositions of sulfides from inactive Tianzuo hydrothermal field, Southwest Indian Ridge: Implications for ultramafic rocks hosting mineralization. *Ore Geology Rev.* 140, 104421. doi: 10.1016/j.oregeorev.2021.104421

Douville, E., Charlou, J. L., Oelkers, E. H., Bienvenu, P., Jove Colon, C. F., Donval, J. P., et al. (2002). The rainbow vent fluids (36°14′N, MAR): the influence ofultramafic rocks and phase separation on trace metal content inMid-Atlantic Ridge hydrothermal fluids. *Chem. Geology* 184, 37–48. doi: 10.1016/S0009-2541(01)00351-5

Firstova, A., Cherkashov, G., Stepanova, T., Sukhanova., A., and Poroshina, I. (2022). New data for the internal structure of ultramafic hosted seafloor massive sulfides (SMS) deposits: case study of the semenov-5 hydrothermal field (13°31′ N, MAR). *Minerals* 12, 1–24. doi: 10.3390/min12121593

Fouquet, Y., Cambon, P., Etoubleau, J., Charlou, J. L., Ondr′eas, H., Barriga, F. J., et al. (2010). "Geodiversity of hydrothermal processes along the Mid-Atlantic Ridge–Ultramafic-hosted mineralization: A new type of oceanic Cu-Zn-Co-Au volcanogenic massive sulfide deposit," in *Diversity of hydrothermal systems on slow spreading ocean ridges*, vol. 321 . Eds. P. A. Rona, C. W. Devey, J. Dyment and B. J. Murton (American Geophysical Union, Washington DC), 367. doi: 10.1029/2008GM000746

Fouquet, Y., Charlou, J. L., Ondréas, H., Radford-Knoery, J., Donval, J. P., Douville, E., et al. (1997). Discovery and first submersible investigations on the Rainbow Hydrothermal Field on the MAR (36°14′N), Eos, Transactions, American Geophysical Union 78, 832. (abstract).

Gao, J. F., Zhou, M. F., Lightfoot, P. C., Wang, C. Y., Qi, L., and Sun, M. (2013). Sulfide saturation and magma emplacement in the formation of the Permian Huangshandong Ni-Cu Sulfide Deposit, Xinjiang, Northwestern China. *Economic Geology* 108, 1833–1848. doi: 10.2113/econgeo.108.8.1833

George, L. L., Cook, N. J., and Ciobanu, C. L. (2016). Partitioning of trace elements in co-crystallized sphalerite-Galena–Chalcopyrite hydrothermal ores. *Ore Geology Rev.* 77, 97–116. doi: 10.1016/j.oregeorev.2016.02.009

George, L. L., Cook, N. J., Crowe, B. B. P., and Ciobanu, C. L. (2018). Trace elements in hydrothermal chalcopyrite. *Mineral Magazine* 82, 59–88. doi: 10.1180/minmag.2017.081.021

German, C. R., Petersen, S., and Hannington, M. D. (2016). Hydrothermal exploration of mid-ocean ridges: where might the largest sulfide deposits be forming? *Chem. Geology* 420, 114–126. doi: 10.1016/j.chemgeo.2015.11.006

Gini, C., Jamieson, J. W., Reeves, E. P., Gartman, A., Barreyre, T., Babechuk, M. G., et al. (2024). Iron oxyhydroxide-rich hydrothermal deposits at the high temperature Fåvne vent field, Mohns Ridge. *Geochemistry Geophysics Geosystems* 25, e2024GC011481. doi: 10.1029/2024GC011481

Graber, S., Petersen, S., Yeo, I., Florent Szitkar, F., Klischies, M., Jamieson, J., et al. (2020). Structural control, evolution, and accumulation rates of massive sulfides in the TAG hydrothermal field. *Geochemistry Geophysics Geosystems* 21, e2020GC009185. doi: 10.1029/2020GC009185

Grant, H. L. J., Hannington, M. D., Pertersen, S., Frische, M., and Fuchs, S. H. (2018). Constraints on the behavior of trace elements in the activity-forming tag deposit, mid-atlantic ridge, based on la-icp-ms analysis. *Chem. Geology* 498, 45–471. doi: 10.1016/j.chemgeo.2018.08.019

Grant, H. L. J., Layton-Matthews, D., and Peter, J. M. (2015). Distribution and controls on silver mineralization in the Hackett River Main Zone, Nunavut, Canada: an Ag- and Pbenriched Archean volcanogenic massive sulfide deposit. *Economic Geology* 110, 943–982. doi: 10.2113/econgeo.110.4.943

Halbach, P., Fouquet, Y., and Herzig, P. (2003). "Mineralization compositional patterns in deep-sea hydrothermal systems," in *Energy mass transfer in marine hydrothermal systems* (Dahlem university press), 85–122. doi: cir.nii.ac.jp/crid/1572543025765604480

Hannington, M. D. (2014). Volcanogenic massive sulfide deposits,in *Treatise on geochemistry*, *2nd ed.* Eds. H. D. Holland and K. K. Turekian (Elsevier, Oxford), 463–488. doi: 10.1016/B978-0-08-095975-7.01120-7

Hannington, M. D., de Ronde, C. E. J., and Petersen, S. (2005). Sea-floor tectonics and submarine hydrothermal systems. *Economic Geology 100th Anniversary* 1905, 111–141. doi: 10.5382/av100.06

Hannington, M., Jamieson, J., Monecke, T., Petersen, S., and Beaulieu, S. (2011). The abundance of seafloor massive sulfide deposits. *Geology* 39, 1155–1158. doi: 10.1130/G32468.1

Hannington, M. D., Jonasson, I. R., Herzig, P. M., and Petersen, S. (1995). "Physical and chemical processes of seafloor mineralization at Mid-Ocean Ridges," in *Seafloor hydrothermal systems: physical, chemical, biological, and geological interactions*. Eds. S. E. Humphris, R. A. Zierenberg, L. S. Mullineaux and R. E. Thomson (American Geophysical Union, Washington DC), 115–157. doi: 10.1029/GM091p0115

Heinrich, C. A., and Eadington, P. J. (1986). Thermodynamic predictions of the hydrothermal chemistry of arsenic and their significance for the paragenetic sequence of some cassiteritearsenopyrite- base metal sulfide deposits. *Economic Geology* 81, 511–529. doi: 10.2113/gsecongeo.81.3.511

Helmy, H. M., Shalaby, I. M., and Rahman, H. A. (2014). Large-scale metal zoning in a late-Precambrian skarn type mineralization, Wadi Kid, SE Sinai, Egypt. *J. Afr. Earth Sci.* 90, 77–86. doi: 10.1016/j.jafrearsci.2013.11.015

Herzig, P. M., Hannington, M. D., and Arribas, A. (1998). Sulfur isotopic composition of hydrothermal precipitates from the Lau back-arc: implications for magmatic contributions to seafloor hydrothermal systems. *Mineralium Deposita* 33, 226–237. doi: 10.1007/s001260050143

Herzig, P. M., Hannington, M. D., Fouquet, Y., von Stackelberg, U., and Petersen, S. (1993). Goldrich sulfides from the Lau Back arc and implications for the geochemistry of gold in sea-floor hydrothermal systems of the Southwest Pacific. *Economic Geology* 88, 2182–2209. doi: 10.2113/gsecongeo.88.8.2182

Hou, K. J., Li, Y. H., and Ye, T. R. (2009). In-situ U-Pb zircon dating laser ablation-multi iron counting-ICP-MS. *Mineral Deposits* 28, 481–492. doi: 10.1360/972008-2143

Humphris, S. E., Herzig, P. M., Miller, D. J., Alt, J. C., Becker, K., Brown, D., et al. (1995). The internal structure of an active sea-floor massive sulfide deposit. *Nature* 377, 713–716. doi: 10.1038/377713a0

Huston, D. L., Sie, S.-H., Suter, G. F., and Cooke, D. R. (1995). Trace elements in sulfide minerals from eastern Australian volcanic-hosted massive sulfide deposits: part I. Proton microprobe analyses of pyrite, chalcopyrite, and sphalerite, and part II. Selenium levels in pyrite: comparison with $\delta^{34}S$ values and implications for the source of sulfur in volcanogenic hydrothermal systems. *Economic Geology* 90, 1167–1196. doi: 10.2113/gsecongeo.90.5.1167

Jamieson, J. W., Clague, D. A., and Hannington, M. D. (2014). Hydrothermal sulfide accumulation along the Endeavour Segment, Juan de Fuca Ridge. *Earth Planetary Sci. Lett.* 395, 136–148. doi: 10.1016/j.epsl.2014.03.035

Jamieson, J. W., Galley, C., McNeil, N., and Mora, D. S. (2023). Evaluating episodicity of high-temperature venting within seafloor hydrothermal vent fields. *Earth Planetary Sci. Lett.* 606, 118051. doi: 10.1016/j.epsl.2023.118051

Jian, H. C., Singh, S. C., Chen, Y. J., and Li, J. B. (2017). Evidence of an axial magma chamber beneath the ultraslow-spreading Southwest Indian Ridge. *Geology* 45, G38351–G38356. doi: 10.1130/G38356.1

Keith, M., Haase, K. M., Klemd, R., Stefan Krumm, S., and Strauss, H. (2016b). Systematic variations of trace element and sulfur isotope compositions in pyrite with stratigraphic depth in the Skouriotissa volcanic-hosted massive sulfide deposit, Troodos ophiolite, Cyprus. *Chem. Geology* 423, 7–18. doi: 10.1080/03717453.2016.1166643

Keith, M., Haase, K. M., Schwarz-Schampera, U., Klemd, R., Petersen, S., and Bach, W. (2014). Effects of temperature, sulfur, and oxygen fugacity on the composition of sphalerite from submarine hydrothermal vents. *Geology* 42, 699–702. doi: 10.1130/G35655.1

Keith, M., Häckel, F., Haase, K. M., Schwarz-Schampera, U., and Klemd, R. (2016a). Trace element systematics of pyrite from submarine hydrothermal vents. *Ore Geology Rev.* 72, 728–745. doi: 10.1016/j.oregeorev.2015.07.012

Kristall, B., Kelly, D., Hannington, M. K., and Deleaney, J. R. (2006). Growth history of a diffusely venting sulfide structure from the Juan de Fuca Ridge: A petrological and geochemical study. *Geochemistry Geophysics Geosystems* 7, 1–30. doi: 10.1029/2005GC001166

Kuznetsov, V., Tabuns, E., Kuksa, K., Cherkashov, G., Maksimov, F., BeĽtenev, V., et al. (2015). The oldest seafloor massive sulfide deposits at the Mid-Atlantic ridge: ^{230}Th/U chronology and composition. *Geochronometria* 42, 100–106. doi: 10.1515/geochr-2015-0009

Lalou, C., and Brichet, E. (1982). Ages and implications of East Pacific Rise sulphide deposits 21°N. *Nature* 300, 169–171. doi: 10.1038/300169a0

Lalou, C., and Brichet, E. (1987). On the isotopic chronology of submarine hydrothermal deposits. *Chem. Geology: Isotope Geosci. Section* 65, 197–207. doi: 10.1016/0168-9622(87)90003-0

Lalou, C., Reyss, J. L., Brichet, E., Arnoldm, M., Thompson, G., Fouquet, Y., et al. (1993). New age data for Mid-Atlantic Ridge hydrothermal sites: TAG and Snakepit chronology revisited. *J. Geophysical Research: Solid Earth* 98, 9705–9713. doi: 10.1029/92JB01898

Lalou, C., Reyss, J. L., Brichet, E., Krasnov, S., Stepanova, T., Cherkashev, G., et al. (1996). Initial chronology of a recently discovered hydrothermal field at 14°45′N, Mid-Atlantic Ridge. *Earth Planetary Sci. Lett.* 144, 483–490. doi: 10.1016/S0012-821X(96)00190-2

Large, R. R., Danyushevsky, L., Hollit, C., Maslennikov, V., Meffre, S., Gilbert, S., et al. (2009). Gold and trace element zonation in pyrite using a laser imaging technique: implications for the timing of gold in orogenic and Carlin-style sediment-hosted deposits. *Economic Geology* 104, 635–668. doi: 10.2113/gsecongeo.104.5.635

Large, R. R., Maslennikov, V. V., Robert, F., Danyushevsky, L. V., and Chang, Z. (2007). Multistage sedimentary and metamorphic origin of pyrite and gold in the Giant Sukhoi log deposit, Lena Gold Province, Russia. *Economic Geology* 102, 1233–1267. doi: 10.2113/gsecongeo.102.7.1233

Li, J. B., Jian, H. C., Chen, Y. S. J., Singh, S. C., Ruan, A. G., Qiu, X. L., et al. (2015). Seismic observation of an extremely magmatic accretion at the ultraslow spreading Southwest Indian ridge. *Geophysical Res. Lett.* 42, 2563–2663. doi: 10.1002/2014GL062521

Li, B., Shi, X. F., Li, C. S., Wang, S., Fan, L., Ye, J., et al. (2024). Subseafloor hydrothermal mineralization in a non-transform offset: Mineralogy and LA-ICP-MS study of sulfide from the Taiji-2 hydrothermal field, Southern Mid-Atlantic Ridge. *Ore Geology Rev.* 167, 105975. doi: 10.1016/j.oregeorev.2024.105975

Li, B., Shi, X. F., Wang, J. X., Yan, Q. S., Liu, C. G., and the DY- Leg, DY- Legs – and DY- Leg Science Parties (2018). Tectonic environments and local geologic controls of potential hydrothermal fields along the southern mid-atlantic ridge (12–14°s). *J. Mar. Syst.* 181, 1–13. doi: 10.1016/j.jmarsys.2018.02.003

Liao, S. L., Tao, C. H., Li, H. M., Barriga, J. A. S. F., Liang, J., Yang, W. F., et al. (2018). Bulk geochemistry, sulfur isotope characteristics of the Yuhuang-1 hydrothermal field on the ultraslow-spreading Southwest Indian Ridge. *Ore Geology Rev.* 96, 13–27. doi: 10.1016/j.oregeorev.2018.04.007

Liao, S. L., Zhu, C. W., Zhou, J. P., Liu, W. ,. Y., iang, J., Yang, W. F., et al. (2021). Distal axis sulfide mineralization on the ultraslow-spreading Southwest Indian Ridge: an LA-ICP-MS study of pyrite from the East Longjing-2 hydrothermal field. *Acta Oceanologica Sin.* 40, 105–113. doi: 10.1007/s13131-020-1681-2

Liu, Z. L., and Buck, W. R. (2018). Magmatic controls on axial relief and faulting at mid-ocean ridges. *Earth Planetary Sci. Lett.* 491, 226–237. doi: 10.1016/j.epsl.2018.03.045

Liu, Y. S., Hu, Z. C., Gao, S., Günther, D., Xu, J., Gao, C. G., et al. (2008). *In situ* analysis of major and trace elements of anhydrous minerals by LA-ICP-MS without applying an internal standard. *Chem. Geology* 257, 34–43. doi: 10.1016/j.chemgeo.2008.08.004

Martin, A. J., Jamieson, J. W., de Ronde, C. E. J., Humphris, S. E., McDonald, I., Layne, G. D., et al. (2023). Trace metal and sulfur cycling in a hydrothermally active arc volcano: deep–sea drilling of the Brothers volcano, Kermadec arc, New Zealand. *Mineralium Deposita* 58, 403–425. doi: 10.1007/s00126-022-01135-x

Maslennikov, V. V., Maslennikova, S. P. M., Large, R. R., and Danyushevsky, L. V. D. (2009). Study of trace element zonation in vent chimneys from the Silurian Yaman-kasy volcanic-hosted massive sulfide deposit (Southern Urals, Russia) using laser ablation-inductively coupled plasma mass spectrometry (LA-ICP-MS). *Economic Geology* 104, 1111–1141. doi: 10.2113/gsecongeo.104.8.1111

Meng, X., Li, X., Chu, F., Zhu, J., Lei, J., Li, Z., et al. (2020). Trace element and sulfur isotope compositions for pyrite across the mineralization zones of a sulfide chimney from the East Pacific rise (1–2°S). *Ore Geology Rev.* 116, 103209. doi: 10.1016/j.oregeorev.2019.103209

Metz, S., and Trefry, J. H. (2000). Chemical and mineralogical influences on concentrations of trace metals in hydrothermal fluids. *Geochimica Cosmochimica Acta* 64, 2267–2279. doi: 10.1016/S0016-7037(00)00354-9

Münch, U., Lalou, C., Halbach, P., and Fujimoto, H. (2001). Relict hydrothermal events along the super-slow Southwest Indian spreading ridge near 63°56′E-mineralogy, chemistry and chronology of sulfide samples. *Chem. Geology* 177, 341–349. doi: 10.1016/S0009-2541(00)00418-6

Nayak, B., Halbach, P., Pracejus, B., and Münch, U. (2014). Massive sulfides of Mount Jourdanne along the super-slow spreading Southwest Indian Ridge and their genesis. *Ore Geology Rev.* 63, 115–128. doi: 10.1016/j.oregeorev.2014.05.004

Petersen, S., and Hein, J. R. (2013). The Geology of Sea-Floor Massive Sulphides [M]//Deep Sea Minerals: Sea-Floor Massive Sulphides, A physical, biological, environmental, and technical review. *Secretariat of the pacific community (SPC), GRID-Arendal, 1A*, 7–18.978-82-7701-119-6

Petersen, S., Herzig, P. M., and Hannington, M. D. (1998). "Fluid inclusion studies as a guide to the temperature regime within the TAG hydrothermal mound, 26°N, Mid-Atlantic Ridge," in *Proc ODP 158, scientific results*. Eds. P. M. Herzig, S. E. Humphris, D. J. Miller and R. A. Zierenberg(College Station, TX) Ocean Drilling Program, 163–178. doi: 10.2973/ODP.PROC.SR.158.210.1998

Petersen, S., Herzig, P. M., and Hannington, M. D. (2000). Third dimension of a presently forming VMS deposit: TAG hydrothermal mound, Mid-Atlantic Ridge, 26°N. *Mineralium Deposita* 35, 233–259. doi: 10.1007/s001260050018

Ren, J. B., He, G. W., Deng, X. G., Deng, X. Z., Yang, Y., and Yao, H. Q. (2022). Metallogenesis of Co-rich ferromanganese nodules in the northwestern Pacific: Selective enrichment of metallic elements from seawater. *Ore Geol Rev.* 143, 104778. doi: 10.1016/j.oregeorev.2022.104778

Ren, J. B., He, G. W., Yang, Y., Yu, M., Deng, Y. N., and Pang, Y. T. (2024). Ultraselective enrichment of trace elements in seawater by Co-rich ferromanganese nodules. *Global Planetary Change* 239, 104498. doi: 10.1016/j.gloplacha.2024.104498

Ren, Y. Q., Wohlgemuth-Ueberwasser, C. C., Huang, F., Shi, X. F., Li, B., Oelze, M., et al. (2021). Distribution of trace elements in sulfides from Deyin hydrothermal field, Mid-Atlantic Ridge – Implications for its mineralizing processes. *Ore Geology Rev.* 128, 103911. doi: 10.1016/j.oregeorev.2020.103911

Román, N., Reich, M., Leisen, M., Morata, D., Barra, F., and Deditius, A. P. (2019). Geochemical and micro-textural fingerprints of boiling in pyrite. *Geochimica Cosmochimica Acta* 246, 60–85. doi: 10.1016/j.gca.2018.11.034

Rouxel, O., Fouquet, Y., and Ludden, J. N. (2004). Subsurface processes at the Lucky Strike hydrothermal field, Mid-Atlantic Ridge: Evidence from sulfur, selenium, and iron isotopes. *Geochimica Cosmochimica Acta* 68, 2295–2311. doi: 10.1016/j.gca.2003.11.029

Scott, S. D., and Barnes, H. L. (1972). Sphalerite-wurtzite equilibria and stoichiometry. *Geochimica Cosmochimica Acta* 36, 1275–1295. doi: 10.1016/0016-7037(72)90049-X

Shalaby, I. M., Stumpfl, E., Helmy, H. M., El Mahallawi, M. M., and Kamel, O. A. (2004). Silver and silver-bearing minerals at the Um Samiuki volcanogenic massive sulphide deposit, Eastern Desert, Egypt. *Mineralium Deposita* 39, 608–621. doi: 10.1007/s00126-004-0427-y

Smith, R. N., and Huston, D. L. (1992). Distribution and association of selected trace elements at the Rosebery Deposit, Tasmania. *Economic Geology* 87, 706–719. doi: 10.2113/gsecongeo.87.3.706

Tao, C. H., Li, H. M., Huang, W., Han, X. Q., Wu, G. H., Su, X., et al. (2011). Mineralogical and geochemical features of sulfide chimneys from the 49°39′ E hydrothermal field on the Southwest Indian Ridge and their geological inferences. *Chin. Sci. Bull.* 56, 2828–2838. doi: 10.1007/s11434-011-4619-4

Tao, C. H., Lin, J., Guo, S. Q., Chen, Y. S. J., Wu, G. H., Han, X. Q., et al. (2012). First active hydrothermal vents on an ultraslow-spreading center: Southwest Indian Ridge. *Geology* 40, 47–50. doi: 10.1130/G32389.1

Tao, C. H., Seyfried, W. E. Jr., Lowell, R. P., Liu, Y. L., Liang, J., Guo, Z. K., et al. (2020). Deep high-temperature hydrothermal circulation in a detachment faulting system on the ultra-slow spreading Ridge. *Nat. Communication* 11, 1300. doi: 10.1038/s41467-020-15062-w

Tivey, M. K., Stakes, D. S., Cook, T. L., Hannington, M. D., and Petersen, S. (1999). A model for growth of steep-sided vent structures on the Endeavour Segment of the Juan de Fuca Ridge: Results of a petrologic and geochemical study. *J. Geophysical Res.* 104, 22859–22883. doi: 10.1029/1999JB900107

Von Damm, K. L. (1995). "Controls on the chemistry and temporal variability of fluids," in Seafloor hydrothermal systems, physical, chemical, biological, and geological interactions. *Geophysical monograph series, The America Geophysical Union* 91, 222–2473. doi: 10.1029/GM091

Wang, Y. J., Han, X. Q., Petersen, S., Frische, M., Qiu, Z. Y., Li, H. M., et al. (2017). Mineralogy and trace element geochemistry of sulfide minerals from the Wocan Hydrothermal Field on the slow-spreading Carlsberg Ridge, Indian Ocean. *Ore Geology Rev.* 84, 1–19. doi: 10.1016/j.oregeorev.2016.12.020

Wang, S., Li, C. S., Li, B., Dang, Y., Ye, J., Zhu, Z. W., et al. (2022). Constraints on fluid evolution and growth processes of black smoker chimneys by pyrite geochemistry: A case study of the Tongguan hydrothermal field, South Mid-Atlantic Ridge. *Ore Geology Rev.* 140, 10440. doi: 10.1016/j.oregeorev.2021.104410

Wang, L. S., Sun, Z. L., Cao, H., Li, H. C., Wang, X. F., Liu, Y. H., et al. (2021). A new method for the U–Th dating of a carbonate chimney deposited during the last glaciation in the northern Okinawa Trough, east China sea. *Quaternary Geochronology* 66, 101199. doi: 10.1016/j.quageo.2021.101199

Wohlgemuth-Ueberwasser, C. C., Viljoen, F., Petersen, S., and Vorster, C. (2015). Distribution and solubility limits of trace elements in hydrothermal black smoker sulfides: An *in-situ* LA-ICP-MS study. *Geochimica Cosmochimica Acta* 159, 16–41. doi: 10.1016/j.gca.2015.03.020

Wood, S. A., and Samson, I. M. (2006). The aqueous geochemistry of gallium, germanium, indium and scandium. *Ore Geology Rev.* 28, 57–102. doi: 10.1016/j.oregeorev.2003.06.002

Yang, W. F., Liao, S. L., Dias, Á., Liang, J., Li, W., Ding, T., et al. (2023). Geochemistry, sulfur and lead isotopic composition of hydrothermal sulfide from the Duanqiao hydrothermal field on the Southwest Indian Ridge: Implications for ore genesis. *Int. Geology Rev.* 65, 883–899. doi: 10.1080/00206814.2022.2081937

Yang, W. F., Tao, C. H., Li, H. M., Liang, J., Liao, S. L., Long, J. P., et al. (2017). $^{230}Th/^{238}U$ dating of hydrothermal sulfides from Duanqiao hydrothermal field, Southwest Indian Ridge. *Mar. Geophysical Res.* 38, 71–83. doi: 10.1007/s11001-016-9279-y

Yeats, C. J., Holli, S. P., Halfpenny, A., Corona, J. C., LaFlamme, C., Southam, G., et al. (2017). Actively forming Kuroko-type volcanic-hosted massive sulfide (VHMS) mineralization at Iheya North, Okinawa Trough, Japan. *Ore Geology Rev.* 84, 20–41. doi: 10.1016/j.oregeorev.2016.12.014

You, C. F., and Bickle, M. J. (1998). Evolution of an active sea-floor massive sulphide deposit. *Nature* 394, 668–671. doi: 10.1038/29279

Yu, J. Y., Tao, C. H., Liao, S. L., Dias, Á.A., Liang, J., Yang, W. F., et al. (2021). Resource estimation of the sulfide-rich deposits of the Yuhuang-1 hydrothermal field on the ultraslow-spreading Southwest Indian Ridge. *Ore Geology Rev.* 134, 104169. doi: 10.1016/j.oregeorev.2021.104169

Yuan, B., Yang, Y. M., Yu, H. J., Zhao, Y. X., Ding, Q. F., Yang, J. C., et al. (2018a). Geochemistry of pyrite and chalcopyrite from an active black smoker in 49.6°E Southwest Indian Ridge. *Mar. Geophysical Res.* 39, 441–461. doi: 10.1007/s11001-017-9324-5

Yuan, B., Yu, H. J., Yang, Y. M., Zhao, Y. X., Yang, J. C., Xu, Y., et al. (2018b). Zone refinement related to the mineralization process as evidenced by mineralogy and element geochemistry in a chimney fragment from the Southwest Indian Ridge at 49.6° E. *Chem. Geology* 482, 46–60. doi: 10.1016/j.chemgeo.2018.01.024

Zeng, Z. G., Ma, Y., Chen, S., Selby, D., Wang, X. Y., and Yin, X. B. (2017). Sulfur and lead isotopic compositions of massive sulfides from deep-sea hydrothermal systems: Implications for ore genesis and fluid circulation. *Ore Geololy Rev.* 87, 155–171. doi: 10.1016/j.oregeorev.2016.10.014

Zhang, H. C., Chen, K., Tao, C. H., Dias, Á., Liang, J., Yang, W. F., et al. (2023). Occurrence and precipitation mechanism of silver in pyrite from chimney fragments in the Edmond hydrothermal field, Central Indian Ridge. *Ore Geology Rev.* 158, 105471. doi: 10.1016/j.oregeorev.2023.105471

Zierenberg, R. A., Fouquet, Y., Miller, D. J., Bahr, J. M., Baker, P. A., Bjerkgård, T., et al. (1998). The deep structure of a sea-floor hydrothermal deposit. *Nature* 392, 485–488. doi: 10.1038/33126